

1 **Aging drives cerebrovascular network remodeling and functional changes in the mouse** 2 **brain**

3
4 Hannah C. Bennett^{1,6}, Qingguang Zhang^{2,6}, Yuan-ting Wu^{1,3}, Uree Chon^{1,4}, Hyun-Jae Pi¹, Patrick
5 J. Drew^{2,5}, Yongsoo Kim^{1,2,7}

6
7 ¹ Department of Neural and Behavioral Sciences, The Pennsylvania State University, Hershey,
8 PA, 17033, USA

9 ² Center for Neural Engineering, Department of Engineering Science and Mechanics, The
10 Pennsylvania State University, University Park, PA, 16802, USA

11 ⁵ Biomedical Engineering, Biology, and Neurosurgery, The Pennsylvania State University,
12 University Park, PA, 16802, USA

13 ⁶ Equal contribution

14 ⁷ Lead contact. Email: yuk17@psu.edu

15
16 Current address:

17 ³ Department of Neurosurgery, Department of Computational Biomedicine, Cedars-Sinai Medical
18 Center, CA 90048

19 ⁴ Stanford University, Stanford, CA 94305

20 21 **Abstract**

22
23 Aging is the largest risk factor for neurodegenerative disorders, and commonly associated with
24 compromised cerebrovasculature and pericytes. However, we do not know how normal aging
25 differentially impacts the vascular structure and function in different brain areas. Here we utilize
26 mesoscale microscopy methods (serial two-photon tomography and light sheet microscopy) and
27 *in vivo* imaging (wide field optical spectroscopy and two-photon imaging) to determine detailed
28 changes in aged cerebrovascular networks. Whole-brain vascular tracing showed an overall
29 ~10% decrease in vascular length and branching density, and light sheet imaging with 3D
30 immunolabeling revealed increased arteriole tortuosity in aged brains. Vasculature and pericyte
31 densities showed significant reductions in the deep cortical layers, hippocampal network, and
32 basal forebrain areas. Moreover, *in vivo* imaging in awake mice identified delays in
33 neurovascular coupling and disrupted blood oxygenation. Collectively, we uncover regional
34 vulnerabilities of cerebrovascular network and physiological changes that can mediate cognitive
35 decline in normal aging.

36 37 **Key Words:**

38 Aging, pericyte, cerebrovasculature, brain, high-resolution mapping, serial two-photon
39 tomography, light sheet fluorescence microscopy, neurovascular coupling

40 41 **Highlight**

- 42 - Brain-wide mapping of vasculature and pericyte changes with normal aging
- 43 - Simplified vascular network with tortuous vessels in aged brains
- 44 - Vascular rarefaction in the deep cortical layers, hippocampus, and the basal forebrain
- 45 - Slowed hemodynamic response in aged animals

46

47 Introduction

48 Aging is the primary risk factor for the development of various neurodegenerative diseases.
49 Notably, aging is associated with decreased cerebral blood flow and general vascular impairment
50 ¹. A common denominator in diseases that increases the risk of dementia, such as stroke,
51 atherosclerosis, and diabetes mellitus, is vascular perturbation and dysfunction of neurovascular
52 coupling ²⁻⁹. All of the disease processes mentioned above increase the risk of developing
53 vascular dementia, which is the second leading cause of cognitive impairment in the United
54 States. Impairment in the cerebrovascular network can have a significant impact on energy
55 supply and metabolic waste removal processes, which can result in neuronal death linked with
56 various clinical symptoms ¹⁰⁻¹². Thus, understanding the anatomical and functional changes in
57 the brain vasculature upon normal aging is a critical first step in understanding
58 neurodegenerative disorders.

59
60 The vessels of the cerebrovascular network are composed of endothelial cells linked by tight
61 junctions. These blood vessels are surrounded by mural cells, such as vascular smooth muscle
62 cells and pericytes, which wrap around vessels of the vascular tree and contribute to blood flow
63 regulation ¹³. Pericytes are essential for maintaining the blood brain barrier and play important
64 roles in waste removal and capillary blood flow regulation ^{14,15}. The importance of these vascular
65 cell types is becoming increasingly recognized in the context of brain disorders, particularly in
66 the case of neurodegenerative diseases. Previous studies showed that aging with cognitive
67 impairment is associated with vascular pathologies including increased arterial tortuosity,
68 rarefaction of the vascular tree, and impairment of pericyte dynamics ^{3,5,14,16-18}. In addition to
69 anatomical changes, advanced aging is associated with reduced cerebral blood flow (CBF),
70 increased CBF pulsatility, and stiffening of the major arteries ¹⁹⁻²¹. It is becoming increasingly
71 recognized that disruption to the brain's vasculature may precede the neuronal damage
72 associated with neurodegenerative disease and other types of dementia ²², implying that vascular
73 dysfunction may play a causative role in neurodegeneration. Despite its significance, it remains
74 unclear how the cerebrovascular network, including mural cell types, across different brain
75 regions undergoes structural and functional changes during the aging process. Prior work has
76 primarily focused on single brain regions without accounting for brain-wide changes in the
77 cerebrovascular network, largely due to the complexities of visualizing and analyzing large 3D
78 brain volumes.

79
80 Recent advances in 3D whole brain imaging methods make it possible to quantitatively examine
81 detailed cerebrovascular networks in the entire mouse brain ²³⁻²⁸. We previously showed that
82 regional differences in pericyte density and cerebrovascular structure strongly correlate with the
83 number of parvalbumin-expressing neuron populations in the cortex of young adult mice ²⁸.
84 Here, leveraging high-resolution 3D mapping methods (light sheet and serial two-photon
85 microscopy), we ask whether there are regional vulnerabilities within the cerebrovasculature and
86 mural cell types upon aging. We found selective reduction of vascular length and pericyte
87 density in deep cortical layers, as well as the basal forebrain areas where cholinergic neurons
88 with large cell bodies reside. Advanced age causes vascular remodeling with increased arterial
89 tortuosity in the isocortex and reduces capillary pericyte density in the entorhinal cortex. In
90 addition to anatomical changes, *in vivo* imaging (two-photon and wide field optical intrinsic
91 signal imaging) of the vasculature in awake aged mice indicates slowed hemodynamic responses

92 to sensory stimulation and voluntary locomotion. Collectively, our results demonstrate
93 significant cerebrovascular network changes, linked to regional vulnerabilities and reduced
94 hemodynamic responsiveness in aging.
95
96
97

98 Results

99

100 Early aging in the mouse brain shows overall decreased vascular length density and 101 branching density, but increased vascular radii

102 To determine structural changes of the cerebrovasculature upon normal aging, we applied our
103 cerebrovascular mapping pipelines in 18-month-old (aged) mice in order to compare 2-month-
104 old (young adult) mice²⁸ (Figure 1). We labeled the brain vasculature by cardiac perfusion of
105 fluorescein isothiocyanate (FITC)-conjugated albumin gel^{26,28-30}. Then, we utilized serial two-
106 photon tomography (STPT) imaging to image the whole mouse brain at 1x1x5 μm resolution
107 (x,y,z ; media-lateral, dorsal-ventral, rostral-caudal) followed by computational analysis for
108 vasculature tracing and quantification^{28,31}. All signals were registered to the Allen Common
109 Coordinate Framework (AllenCCF) as a reference brain³² (Figure 1).

110 To identify potential regional vascular vulnerabilities, we first examined the overall
111 changes of the cerebrovasculature across the whole mouse brain, comparing 18-month-old mice
112 to 2-month-old mice (Figure 2A). Total vessel length in most regions remained similar between
113 18- and 2-month-old mice (Figure 2B) but overall brain volume increased about 6% (Figure 2C).
114 The brain volume increase was also seen with *in vivo* longitudinal MRI³³, indicating our result is
115 not an artifact from fixation or imaging. As a result, overall vascular length density across
116 different brain regions decreased by 5 – 10% in the aged brain (Figure 2D). In addition, we
117 found an approximate 10-20% decrease in branching density across most brain regions (Figure
118 2E). In contrast, the average radius of 18-month-old mouse brain vasculature is increased by
119 about 5 – 10% compared to 2-month-old mice, suggesting reduced basal constrictive tone
120 (Figures 2F). Notably, we found significant changes in brain regions related to memory
121 processing and storage (e.g., Ammon's horn; CA, lateral entorhinal cortex; ENTI, Anteromedial
122 nucleus; AM), appetitive behavior (e.g., medial preoptic area; MPO, ventral premammillary area;
123 PMv), body physiology and sleep (e.g., lateral preoptic area; LPO, anterior hypothalamic area;
124 AHA), attention (e.g., substantia innominata; SI, medial septum; MS as basal forebrain areas),
125 sensory processing and integration (e.g., zona incerta; ZI, Dorsal lateral geniculate nucleus; LGd),
126 and executive function (e.g., medial group of the dorsal thalamus; MED) (Figure 2D-F,
127 highlighted with magenta boxes; Supplementary Data 1).

128 Next, we examined isocortical areas for aging-related vascular changes. Surprisingly,
129 isocortical areas showed no significant changes, with mostly less than 10% decrease in length
130 and branching density, and about 5% increase in average vessel radius (Figure 2G-I). To
131 examine vascular changes in the isocortex more intuitively, we utilized our previously developed
132 isocortical flatmap with five distinct cortical domains marked by different colors (Figure 2J)²⁸.
133 We found a significant reduction in vessel length density only in layer 6 of aged brains compared
134 to young brains (Figure 2K-N). Our result corroborates a previous finding showing selective
135 vulnerability of deep cortical layers³⁴. Together, these findings indicate that the vasculature of
136 the isocortex is relatively resilient to aging, and the earliest evidence of age-related vascular
137 degeneration occurs in layer 6.

138

139 Pericyte density in aged brains showed significant decrease in basal forebrain regions and 140 the deep cortical layer.

141 Pericytes are a mural cell type that plays a key role in the regulation of the capillary network
142 blood flow and diameter, and are known to be vulnerable in aging^{15,35,36}. Our results show
143 increased vascular radius in aged brains, which raises the possibility of dysfunction in pericytes

144 in the maintenance of vascular diameter. To quantitatively determine changes of pericytes, we
145 compared capillary pericyte densities in 2-month-old and 18-month-old PDGFR β -Cre;Ai14 mice
146 ^{37,38}, where tdTomato is expressed in pericytes and other mural cells. We used STPT imaging of
147 PDGFR β -Cre;Ai14 mice with previously developed computational analyses to image, identify,
148 and quantify changes of capillary pericytes upon aging across the whole mouse brain ^{28,31} (Figure
149 1 bottom and Figure 3A).

150 Overall, pericyte density in the aged brain remained within 10% of that in young brains in
151 most areas, including many cortical and thalamic subregions (Figure 3B; Supplementary Data 2).
152 However, a significant reduction of pericyte density was found in basal forebrain areas (e.g., the
153 substantia innominata; SI, magnocellular nucleus; MA) and the closely related anterior amygdala
154 area (AAA) (Figures 3B; red boxed, C-D) ³⁹. Considering the basal forebrain contains cortical-
155 projecting cholinergic neurons, the observed significant reduction in pericyte and vascular
156 densities reflects the selective and early vulnerability of the basal forebrain during aging. These
157 results could potentially provide a link between known vascular impairment and dysfunction of
158 cholinergic neurons in neurodegenerative diseases such as Alzheimer's disease ^{40,41}.

159 Given that we saw few vascular changes with aging in the isocortex (Figure 2), we
160 investigated whether this resilience extends to pericyte density. We compared 2-month- and 18-
161 month-old mice capillary pericyte densities by brain region using our isocortical flatmap (Figure
162 3E). The capillary pericyte density in aged mice overall remained similar to, or even slightly
163 increased as compared with young adult mice (Figure 3E-F), particularly in motor sensory
164 regions (white and gray arrowheads in Figure 3E). Due to reduced vessel length density, the
165 overall pericyte cell body coverage (capillary pericyte number per vascular length) is increased
166 by about 10% in sensorimotor areas in aged mice compared to young adult mice (Figure 3G). In
167 contrast to sensorimotor areas, relatively little or even reduced pericyte coverage was observed in
168 medial prefrontal areas, suggesting selective reduction of pericytes with aging in an association
169 area known to be related to higher cognitive functions.

170 We then asked whether there are selective changes across cortical layers. We noted that
171 the deep cortical layer (L6) showed selective reduction of pericyte density in the infralimbic
172 cortex, while the superficial layers (2/3 and 4) in the whisker representation of the primary
173 somatosensory cortex ('barrel field') showed a significant increase in the 18-month-old brain
174 compared to the 2-month-old brain (Figure 3H-J). When layer specific density from all
175 isocortical areas was combined, pericyte density was significantly reduced in deep layer 6b in the
176 aged brain, while layers 2/3 and 4 showed significant increases (Figures 3K). Considering layer
177 6b plays a role in brain state modulation ⁴² and the protective role of pericytes in vascular
178 integrity, significant reduction of the pericytes could make layer 6b and nearby white matter
179 tracks more vulnerable upon aging.

180 181 **Artery specific labeling shows striking vascular remodeling in penetrating cortical** 182 **arterioles of aged brains.**

183 Previous studies have identified age-related changes in arteries and arterioles in both rodents and
184 humans ^{43,44}. To investigate potential remodeling in main arteries and penetrating cortical
185 arterioles, we utilized tissue clearing, 3D immunolabeling, and high-resolution light sheet
186 fluorescence microscopy (LSFM) imaging (Figure 4A) (Methods for more details). We labeled
187 arteries with smooth muscle actin (Acta 2) and transgelin (Sm22) antibodies, pan-vasculature
188 with lectin, and pericytes with CD13 and PDGFR β antibodies in the same brain. This approach

189 enabled us to examine different vascular compartments and mural cell types in the same intact
190 3D brain (Figure 4B-H).

191 We applied the method to 2-month-old and 24-month-old (late aging) C57BL/6 mice to
192 test whether late aging shows structural remodeling of different vascular compartments and
193 progression of capillary pericyte density reduction. We first focused our analysis on the middle
194 cerebral artery and anterior communicating artery branches contributing to the anterior
195 circulation of the circle of Willis, which is responsible for supplying the majority of cerebral
196 blood flow (Figure 5A). We quantified the average radius of each artery. We did not find
197 significant differences in young and aged mice, nor differences between sexes (Figure 5B-C),
198 suggesting that aging does not impact the diameters of the main feed arteries to the brain.

199 Next, we examined the number of cortical penetrating arterioles, which are bottlenecks in
200 the supply of blood to the brain^{45,46}. There were no significant changes in cortical arteriole
201 numbers (both total arterioles and arterioles that extend into layer 6/corpus callosum) in aged
202 brains compared to the young adult mice (Figure 5D). However, we observed highly tortuous
203 (twisted) vessels across the entire cortex (Figure 5E; highlighted with red arrowheads), which is
204 consistent with prior observations in aged animals and humans^{47,48}. Further analysis revealed
205 that aged animals demonstrate increased arteriole tortuosity, as measured by the arc chord ratio
206 (Figure 5F) (see Methods for more details). The number of branching points per arteriole
207 remains similar across the age group (Figure 5G). This increased tortuosity of penetrating
208 arterioles will result in increased blood flow resistance, leading to slowed blood flow with
209 decreased oxygen and nutrient delivery if there is no increase in blood pressure. This decreased
210 flow could make the deep cortical layers and nearby white matter tracks vulnerable during aging.

211
212 **Advanced aging is associated with selective loss of capillary pericytes in cortical layer 6 and**
213 **the entorhinal cortex.**

214 Different pericyte subtypes associate with different vascular branches (Figure 5H)¹³. Aging has
215 been shown to impair specific pericyte subtypes, such as first order (ensheathing) pericytes at the
216 junction between arterioles and microvessels⁴⁹. To examine how different pericyte subtypes are
217 differentially impacted in advanced aging, we used a combination of artery, pan-vascular, and
218 mural cell immunolabeling, in order to distinguish pericyte subtypes at different vascular zones
219 with submicron resolution ($0.4 \times 0.4 \times 1 \mu\text{m}^3$) using LSFM imaging (Figure 5I). We successfully
220 visualized individual pericytes and their subtypes, including capillary pericytes, both mesh and
221 thin-strand morphologies, and ensheathing pericytes, which are located along pre-capillary
222 arterioles and express smooth muscle markers such as Acta2³⁴ (Figure 5H-I). Examples of
223 different pericyte subtypes (i.e., ensheathing, mesh, and thin strand) are labeled in Figure 5I with
224 cyan, yellow, and purple arrows in each panel, respectively. By following individual vasculature,
225 each pericyte type was manually counted in a region of interest.

226 Consistent with our STPT data, we did not observe any significant changes in pericyte
227 subtype density within the primary somatosensory cortex except a significant reduction of
228 capillary pericyte density in layer 6 (Figure 5J-L). This result further confirmed that pericyte
229 density remains largely unchanged in cortical areas, including contractile ensheathing pericytes.
230 We further examined the entorhinal cortex, since this region is important for memory and is
231 known to be very sensitive to age-related diseases^{4,18,35,50-52}. While this region did not show any
232 statistically significant decreases at 18 months of age (early aging) in STPT pericyte mapping
233 (Figure 3B), we found that both mesh and thin-strand pericytes, but not ensheathing pericytes,

234 showed significant reductions in 24-month-old (late aging) mice (Figure 5M-N). This suggests
235 that capillary pericytes are at higher risk of cellular density loss, particularly in advanced age.
236

237 ***In vivo* imaging to examine hemodynamic changes in aged brains.**

238 In addition to structural changes, the cerebrovasculature may undergo functional changes in
239 neurovascular coupling with aging. Thus, we investigated how normal aging impacts brain
240 hemodynamics during rest and in response to voluntary locomotion and sensory stimulation in
241 awake behaving mice, using wide field intrinsic optical imaging of spectroscopy (IOS)⁵³ and
242 two-photon laser scanning microscopy (2PLSM)⁵⁴⁻⁵⁶ (Figure 6 and 7). All experiments were
243 performed in awake mice that were head-fixed on a spherical treadmill for voluntary locomotion
244⁵³⁻⁵⁷. Imaging was performed through polished and reinforced thin-skull windows (PoRTS) to
245 minimize the disruption of the intracranial environment⁵⁸. We utilized two different models,
246 voluntary locomotion^{53,55} and whisker stimulation^{54,56,59}, to quantify the evoked responses. We
247 focused our analysis on two functionally distinct cortical regions, the forelimb/hindlimb
248 representation of the somatosensory cortex (FL/HL) and a frontal cortical region (FC) including
249 the anterior lateral motor cortex (ALM). We targeted ALM because it is involved in motor
250 planning and performs “higher-order” cognitive functions in mice, which makes it analogous to
251 the human prefrontal cortex. We performed these measurements in mice of ages of 2-4 month,
252 18 month, and 24 month.
253

254 **Neurovascular coupling shows slower response time in aged brains.**

255 We first assessed the spatial extent of cortical hemodynamic responses and their relationship to
256 voluntary locomotion, using intrinsic optical signal imaging of spectroscopy⁵³. Taking
257 advantage of differences in the optical absorption spectra of oxyhemoglobin (HbO) and
258 deoxyhemoglobin (HbR)^{60,61}, we collected reflectance images during rapid alternating green
259 (530 nm) and blue (470 nm) illumination (Figure 6A and H). When the brain is illuminated with
260 light of different wavelengths, increases in total hemoglobin concentration (ΔHbT) in turn report
261 dilations of arteries, capillaries, and veins, which correspond with increases in cerebral blood
262 volume (CBV). The ΔHbT observed with IOS closely tracks measurements of vessel diameter
263 made with two-photon microscopy⁶². The consistency of microscopic measurements of vessel
264 diameter, combined with its very high signal-to-noise ratio⁵⁴, and spatial resolution (less than
265 200 μm)⁶³, makes IOS suitable for detecting hemodynamic responses to locomotion. While
266 neurally-evoked dilations initiate in the deeper layers of the cortex, the dilations propagate up the
267 vascular tree to the surface arteries⁶⁴⁻⁶⁷, where they can be easily detected with IOS.

268 We quantified how locomotion affected CBV in two complementary ways. We calculated
269 the locomotion-triggered average, generated by aligning the IOS or vessel diameter signals to the
270 onset or offset of locomotion using only locomotion events ≥ 5 seconds in duration (Figure 6B
271 and C). Using changes in ΔHbT as an indicator of CBV, we observed region-specific changes in
272 ΔHbT during locomotion (Figure 6B and C). In young adult mice (2-4 months old), there was a
273 pronounced increase in the ΔHbT (corresponding to an increase in CBV) in the
274 forelimb/hindlimb representation of the somatosensory cortex (FL/HL), while in the frontal
275 cortex (FC) there was no change, or even a slight decrease in ΔHbT ($n = 7$ mice) (Figure 6B and
276 C), consistent with previous reports^{53,57,68}. This pattern was not affected by aging, as we
277 observed similar results in 18-month-old ($n = 5$ mice) and 24-month-old ($n = 11$ mice) (Figure
278 6B and C).

279 We also calculated the hemodynamic response function (HRF)^{54,69}, which is the linear
280 kernel relating locomotion events to observed changes in CBV and vessel diameter (Figure 6D
281 and F; see Methods), using all locomotion events. Hemodynamic response functions are used in
282 all of fMRI analyses to extrapolate neuronal activity from a stimulus or a task from
283 hemodynamic signals, and take into account the slower responses of the vasculature relative to
284 neurons⁷⁰. Using the HRFs to quantify the net CBV, we obtained the same conclusions as
285 derived from the locomotion-triggered average, i.e., the net increase in cerebral blood volume
286 does not change during aging (Figure 6E and G, left) in either FC or FL/HL (2-month: $0.53 \pm$
287 $0.18 \mu\text{M}$; 18-month: $0.57 \pm 0.06 \mu\text{M}$; 24-month: $0.53 \pm 0.12 \mu\text{M}$). In addition to the amplitude of
288 the hyperemic response evoked by locomotion, HRFs also provide us information regarding the
289 temporal dynamics of CBV responses. We found that the onset time (Figure 6E, middle, 2-month:
290 $0.95 \pm 0.15 \text{ s}$; 18-month: $0.95 \pm 0.14 \text{ s}$; 24-month: $1.17 \pm 0.10 \text{ s}$) and duration (Figure 6E, right,
291 2-month: $1.11 \pm 0.12 \text{ s}$; 18-month: $1.24 \pm 0.24 \text{ s}$; 24-month: $1.38 \pm 0.24 \text{ s}$) of locomotion evoked
292 hyperemic response is significantly lengthened with aged brains, especially in the late aging
293 groups (22-26 month old) in the FL/HL (2-4 month vs 22-26 month: time to peak, unpaired t-test,
294 $t(14) = 3.54$, $p = 0.0033$; FWHM, Wilcoxon rank sum test, $p = 0.0311$). To further validate the
295 results from HRFs, we quantified the responses of ΔHbT in response to a brief whisker
296 stimulation (100 ms duration) (Figure 6H). We observed that in response to contralateral whisker
297 stimulation, the onset time and duration of ΔHbT response are significantly lengthened in the 24-
298 month-old late aging groups in both FC and FL/HL (Figure 6I-L).

299 In addition to the mesoscopic level measurements using IOS, we further compared
300 whether hemodynamics was different between age groups at individual vessel level in FL/HL, in
301 terms of pial arterial diameter change in response to locomotion, using *in vivo* 2PLSM (Figure
302 6M). The locomotion-evoked arterial diameter change (Figure 6N), as well as the HRF of arterial
303 diameter change (Figure 6O) showed a similar spatial pattern of responses as the CBV measured
304 using IOS, i.e., a trend of delayed response during aging.

305 Finally, to determine whether vascular dilation capacity was intact in aged mice, we
306 measured the mesoscopic brain hemodynamic responses using IOS (Figure 6P) and microscopic
307 vessel diameter response to isoflurane, a potent vasodilator, using 2PLSM. In FL/HL, we
308 observed an increase of ΔHbT (2-month: $176.8 \pm 29.5 \mu\text{M}$, 4 mice; 18-month: $146.7 \pm 22.2 \mu\text{M}$,
309 4 mice; 24-month: $133.8 \pm 23.5 \mu\text{M}$, 5 mice) and arteriole diameter (2-month: $65.5 \pm 19.2\%$, 4
310 mice; 18-month: $51.7 \pm 10.8\%$, 5 mice; 24-month: $54.6 \pm 28.9\%$, 8 mice; data not shown) when
311 animals inhale isoflurane. In FC, we observed an increase of ΔHbT (2-month: $106.6 \pm 28.5 \mu\text{M}$,
312 4 mice; 18-month: $85.4 \pm 23.0 \mu\text{M}$, 4 mice; 24-month: $93.6 \pm 18.2 \mu\text{M}$, 5 mice). The extent of
313 vasodilation observed between young and old mice was not different when animals were
314 transitioned from air to 5% isoflurane, suggesting the dilation capacity remains similar across
315 different age groups.

316 317 **Oxygenation carrying capacity is decreased in aged mice.**

318 One of the important functions of increased blood flow/volume is to deliver oxygen to the brain.
319 Using the cerebral oxygenation index (HbO-HbR)^{53,71}, a spectroscopic measurement of
320 hemoglobin oxygenation, we saw an increase in oxygenation during locomotion and whisker
321 stimulation in both FC and FL/HL areas in young mice. The oxygen increase in response to
322 locomotion (Figure 7A) and whisker stimulation (Figure 7B) did not significantly differ across
323 age groups. As vasodilation is one of the determining factors controlling brain oxygenation⁵³,
324 we quantified the relationship between locomotion evoked responses of ΔHbT and $\Delta\text{HbO-HbR}$

325 using linear regression. The slope and intercept of the fitting decreased with the healthy aging
326 process (2-month: $y = 0.8667x + 35.43$; 18-month: $y = 0.5209x + 27.37$; 24-month: $0.5885x +$
327 30.42 ; Figure 7C), which suggests that oxygen carrying capacity for the red blood cells decreases
328 during aging, and that the aging brain has lower baseline oxygenation, respectively.

329 To determine whether the oxygen exchange and oxygen delivery capacity were intact in
330 aged mice, we measured the brain tissue oxygenation response when mice breathed 100%
331 oxygen (Figure 7D-G). We observed that the oxygen delivered to the brain is significantly
332 smaller in the aged mouse brain, both in the FC (2-month: $43.7 \pm 4.1 \mu\text{M}$; 18-month: 32.5 ± 10.4
333 μM ; 24-month: $27.0 \pm 9.5 \mu\text{M}$. Linear mixed effects model, $p = 0.0078$) and FL/HL (2-month:
334 $71.0 \pm 14.4 \mu\text{M}$; 18-month: $51.0 \pm 5.3 \mu\text{M}$; 24-month: $35.5 \pm 21.7 \mu\text{M}$. Linear mixed effects
335 model, $p = 0.0032$).

336 Lastly, we quantified the functions of the brain capillary network during aging progress,
337 as its dynamics affect brain oxygenation responses^{53,72}. We first compared whether red blood
338 cell (RBC) velocity differed between age groups in the capillary network. We found no
339 significant differences in lumen diameter between different groups (2-month: $4.7 \pm 1.65 \mu\text{m}$, 32
340 capillaries; 18-month: $4.9 \pm 1.2 \mu\text{m}$, 36 capillaries; 24-month: $3.6 \pm 1.0 \mu\text{m}$, 56 capillaries), a
341 trend toward decreased RBC velocity, but not a statistically significant difference (2-month: 0.58
342 $\pm 0.33 \text{ mm/s}$; 18-month: $0.53 \pm 0.34 \text{ mm/s}$; 24-month: $0.34 \pm 0.25 \text{ mm/s}$) (Supplementary Figure
343 1A), no difference in hematocrit (2-month: $38.3 \pm 7.6\%$; 18-month: $33.4 \pm 9.6\%$; 24-month: 34.5
344 $\pm 9.7\%$; Supplementary Figure 1B). In addition to RBC flow rate and hematocrit, the “stochastic”
345 nature of red blood cell distribution in the capillary also affects brain oxygenation^{55,72}. When we
346 quantified the spacing of RBC and the occurrence of “stall” events, we found no significant
347 difference between different aging groups (Supplementary Text 1).

348 Collectively, our *in vivo* recording results suggest slowed vascular response dynamics
349 and decreased oxygen carrying capacity in normal aging, which can create imbalances in
350 baseline and on demand supply of energy and oxygen in aged brains.

351
352
353
354

355 Discussion

356
357 Understanding structural and functional changes of the cerebrovasculature during normal aging
358 will provide foundational information to understand altered brain energy infrastructure that can
359 be commonly linked with many neurodegenerative disorders. Here, we provide detailed
360 information regarding anatomical changes of the cerebrovascular network and physiological
361 alteration of the blood flow in aged mouse brains, as summarized in Figure 8. We found overall
362 reductions in vascular length and branching densities, along with tortuous arterioles that indicate
363 sparser and remodeled vascular networks in aged brains. We also uncovered selective vascular
364 and pericyte loss in cortical deep layers, basal forebrain regions, and the hippocampal network,
365 including the entorhinal cortex, which may contribute to their regional vulnerabilities in
366 neurodegenerative disorders^{41,73}. Lastly, our *in vivo* studies showed delayed neurovascular
367 coupling response time and inefficient oxygen delivery in aged brains. Collectively, our results
368 advance our understanding of global changes and regional vulnerabilities associated with
369 deteriorating vascular networks in aged brains.

371 Cerebrovascular structural changes with selective pericyte reduction in aged brains.

372 Previous studies in aged cerebral vasculature have shown stiffened arteries, microvascular
373 rarefaction, and remodeled vascular trees in selected brain regions^{16,19,74–76}. Our study showed
374 that there is an approximate 10% decrease in overall vascular density, as well as branching
375 density, in 18-month-old compared to 2-month-old mouse brains, suggesting a sparser vascular
376 network to distribute the blood³³. Moreover, aged brains showed substantially more tortuous
377 penetrating arterioles, which impede blood flow by increasing flow resistance. This increase in
378 resistance, unless countered by an increase in blood pressure, could result in reduced oxygen and
379 nutrient supply, particularly in distal areas from main arteries such as the deep cortical layers and
380 white matter tracks^{19,77}. Importantly, human studies have shown similar changes with tortuous
381 vasculature and slowed cerebral blood flow^{21,75,78,79}. Such changes can lead to an increased heart
382 rate to compensate for cerebral hypoperfusion, as frequently observed in elderly population⁸⁰.
383 We also found an overall increase in average vessel radii. Notably, pericytes are known to
384 regulate the basal tone of microvessels^{13,15}, and a recent study showed that pericytes in
385 superficial cortical layers have impaired recovery of cellular processes in the aged brain³⁴.
386 Therefore, while pericyte cell density does not change significantly during aging, their regulatory
387 function may be impaired, resulting in slightly dilated cerebrovasculature.

388 Our data showed that the vasculature of the isocortex is more resilient to aging compared
389 to other brain regions, as evidenced by no significant changes in both microvascular and
390 capillary pericyte densities. However, deep cortical layers, especially layer 6b, showed reduced
391 vessel density and pericyte density, consistent with previous studies⁸¹. Notably, layer 6 plays a
392 crucially important role as the output layer to the thalamus^{42,82}. Moreover, layer 6b is the only
393 cortical layer that is responsive to sleep-wake neuropeptides such as orexin, which is produced in
394 the lateral hypothalamus^{82,83}. Considering that sleep is often dysregulated with increased age in
395 humans⁸⁴, failing cerebrovascular network in the deep cortical layer may provide important
396 insight to understand aging related sleep dysregulation.

397 Since our 3D mapping data examine vascular network changes of the whole mouse brain
398 in an unbiased way, we identified specific brain regions with selective vulnerabilities in aged
399 brains. For example, we found significantly reduced vascular and pericyte densities in the basal
400 forebrain area, which contains cholinergic neurons⁸⁵. The basal forebrain cholinergic neurons

401 (BFCNs) have highly extensive projections to the cortical area and have large soma size with
402 high energy demands⁸⁶. Previous clinical and preclinical studies have shown that BFCNs are
403 highly vulnerable in Alzheimer's disease (AD) and their deterioration is linked with memory
404 impairment^{41,87}. Impaired vascular networks with decreased pericyte density may, potentially
405 serve as an underlying cause of BFNC degeneration in normal aging and neurodegenerative
406 disorders, including AD^{73,88,89}. Another notable area is the entorhinal cortex (ENT), a part of the
407 hippocampal network, which has been heavily implicated in AD and particular cognitive deficits
408^{90,91}. The lateral ENT (ENTl) showed significantly decreased vascular length, branching point,
409 and capillary pericyte density. The ENTl vascular density is one of lowest across the brain region
410 in normal adult mice²⁸. With additional decreases with aging, blood supply in the ENTl is likely
411 to be highly limited and less able to withstand further insult, which may explain its vulnerability
412 to neurodegenerative disorders. Lastly, our study identified specific thalamic and hypothalamic
413 areas with decreases in the vascular network density, such as the medial preoptic area, which
414 warrant future studies for these largely understudied subcortical areas in aging research.

415

416 **Slowed neurovascular response and decreased oxygen in aged brains.**

417 In addition to anatomical changes, we found slowed brain hemodynamic responses during
418 locomotion and whisker stimulation in aged mice, while the amplitude of blood increase
419 remained intact. This suggests that the aged brain can still deliver enough red blood cells to the
420 regions with energy demands, but the timing of the delivery is perturbed. Interestingly, the
421 slowed hemodynamic response is also observed when noradrenergic input from the locus
422 coeruleus is disrupted⁹², consistent with the disruption of the locus coeruleus having a role in
423 Alzheimer's disease and dementia⁹³. Moreover, the baseline oxygenation and oxygen carrying
424 capacity of the red blood cells decrease with age^{94,95}. Notably, respiration is an important
425 regulator of brain oxygenation⁵³, and lung function decreases during the aging process^{96,97}. The
426 decreased ability to deliver oxygen can also be related to decreased microvessel density and its
427 connectivity, resulting in less effective oxygen distribution, and the shift of the oxyhemoglobin
428 dissociation curve with age⁹⁴. This baseline drop in brain oxygenation will make the brain more
429 vulnerable to hypoxia when facing increased oxygen demand, as neurons become hyperexcitable
430 in aged brains⁹⁸⁻¹⁰⁰. This baseline drop in brain oxygenation, in combination with increased
431 blood flow resistance, due to increased vessel tortuosity and reduced vascular density, will make
432 brain areas in distal vascular territories, such as white matter tracks, and watershed areas
433 (located at the junction between main artery territories) selectively vulnerable in aged brains
434^{21,101}. Finally, as neurovascular coupling potentially serves many other functions besides oxygen
435 delivery, disruption of the normal hemodynamic response may have other adverse physiological
436 effects¹⁰².

437

438 **Limitations of the Study**

439 In our anatomical studies, we found significant vascular loss in deep cortical areas and many
440 subcortical areas (e.g., basal forebrains, hypothalamus, and entorhinal cortex). However, our *in*
441 *vivo* measurement is limited to superficial cortical layers, where we did not observe dramatic
442 anatomical changes. Although the brain hemodynamics at the surface reflect the dynamics along
443 the vascular tree, future studies with emerging techniques such as functional ultrasound imaging
444 or three-photon microscopy imaging will help to address functional changes in these important,
445 yet hard-to-reach brain areas^{103,104}. Moreover, our analysis mostly focuses on the arterial and

446 capillary compartments of the vasculature. Future studies are needed to elucidate how aging
447 affects the structure and function of the venous side of aged brains.

448

449 **Summary**

450 Taken together, our study reveals aging-related brain-wide and area-specific changes in vascular
451 and mural cell types. These changes can explain the vulnerability and resilience of different brain
452 areas in normal aging. Moreover, we identified an age-related decrease in brain oxygenation and
453 delayed neurovascular coupling, which can be linked with cognitive impairment in aged brains.
454 These aging-related changes will serve as a common factor in understanding many
455 neurodegenerative disorders and cognition decline in the elderly population.

456

457

458

459

460

461 **Acknowledgments**

462 We thank Josephine Liwang for constructive discussion of the manuscript, Dr. Volkhard Linder
463 for kindly sharing PDGFR β -Cre transgenic mice and Dr. Zhuhao Wu for sharing tissue clearing
464 protocol. We thank Jen Minter and Becca Betty for valuable management of our animal colony,
465 as well as the coding support provided by Fae Kronman. We acknowledge the use of
466 computational resources in the High Performance Computing cluster at the Penn State College of
467 Medicine.

468 **Funding:**

469 National Institutes of Health grant R01NS108407 and RF1MH12460501 (YK)

470 National Institutes of Health grant R01NS078168 and R01NS101353 (PJD)

471 American Heart Association Career Development Award #935961 (QZ)

472 Its contents are solely the responsibility of the authors and do not necessarily represent the views
473 of the funding agency.

474

475

476 **Author Contributions**

477 Conceptualization: YK, HCB

478 Data Collection: HCB, UC, YK

479 Developing Computational Analysis: YTW

480 Data Analysis: HCB, QZ, YTW, HP, YK

481 *In vivo* imaging: QZ, PJD

482 Manuscript preparation: HCB, YK, QZ with help from other authors.

483

484 **Declaration of Interests**

485 The authors declare no competing interests.

486

487
488
489
490
491
492
493
494
495
496
497
498
499
500
501
502

RESOURCE AVAILABILITY

Lead contact

Further information and requests for resources should be directed to and will be fulfilled by the lead contact, Yongsoo Kim (yuk17@psu.edu).

Materials availability

This study did not generate new unique reagents.

Data and code availability

All dataset and codes can be used for non-profit research without any restriction. Any additional information required to reanalyze the data reported in this paper is available from the lead contact upon request.

503 **METHODs**

504

505 **Animals**

506 Animal experiments were approved by the Institutional Animal Care and Use Committee at Penn
507 State University. Adult male and female mice were used across all age and genotype groups in
508 this study. For transgenic pericyte-specific experiments, PDGFR β -Cre mice (a kind gift from the
509 Volkhard Lindner Lab)³⁷ were crossed with female Ai14 mice which express a Cre-dependent
510 tdTomato fluorescent reporter (LoxP-Stop-LoxP-tdTomato). These PDGFR β -Cre: Ai14 mice
511 exhibit PDGFR β expression in two distinct mural cell types, pericytes and vascular smooth
512 muscle cells. Both the adult 2-month-old and 18-month-old PDGFR β -Cre: Ai14 mice were bred
513 and aged in house. We used tail genomic DNA with PCR for the transgenic mouse lines
514 requiring genotyping. Adult 2-month-old C57BL/6J mice were bred from C57BL/6J mice
515 directly obtained from the Jackson Laboratory and used for vascular tracing experiments with
516 FITC filling (n=4)²⁸. 18-month-old C57BL/6J mice utilized for FITC-fill vascular mapping
517 experiments were aged from a local C57BL/6 mouse colony. 24-month-old C57BL/6J mice used
518 for the current study were directly obtained from the National Institute of Aging at 18 months
519 and aged to 24 months in house. All animals were used once to generate data, and aged animals
520 with tumors or other appreciable abnormalities were excluded from analysis.

521 For the *in vivo* two-photon imaging experiments, a total of 31 C57BL/6J mice of both
522 sexes (2-26 months old, 18-35 g, Jackson Laboratory) were used. Recordings of cerebral blood
523 volume and cerebral oxygenation response to locomotion were made from 23 mice (2-4 month
524 old: n = 7 mice; 18 month old: n = 5 mice; 22-26 month old: n = 11 mice) using wide field
525 optical imaging. In a subset of the mice (2-4 month old: n = 5 mice; 22-26 month old: n = 5
526 mice), we also recorded cerebral blood volume and cerebral oxygenation response to whisker
527 stimulus using optical imaging. Recordings of stacks, capillary blood flow velocity, and
528 diameters of arteries and veins using two-photon laser scanning microscopy (2PLSM) were
529 conducted in 23 mice (15 of these 23 mice were also used for wide field optical imaging; 2-4
530 month old: n = 10 mice; 18 month old: n = 5 mice; 22-26 month old: n = 8 mice). Mice were
531 given food and water *ad libitum* and maintained on 12-hour (7:00–19:00) light/dark cycles. All
532 experiments were conducted during the light period of the cycle.

533

534 **Perfusion based vascular labeling, STPT imaging, and computational analysis**

535 Overall procedure remains similar to our previous publication²⁸. The detailed procedure has
536 been included in a separate protocol paper³¹. Briefly, animals were deeply anesthetized with
537 ketamine-xylazine, and perfused with 1X PBS followed by 4% paraformaldehyde to wash out
538 blood and allow for tissue fixation, respectively. For vessel labeling, immediately following 4%
539 paraformaldehyde, 0.1% (w/v) fluorescein isothiocyanate (FITC)-conjugated albumin (Sigma-
540 Aldrich, cat.no.: A9771-1G) in a 2% (w/v) solution of porcine skin gelatin (Sigma-Aldrich,
541 cat.no.: G1890-500G) was perfused to obtain vascular filling. For STPT imaging, the brain
542 sample was embedded in oxidized agarose and cross-linked in 0.05M sodium borohydrate at 4°C
543 for at least 2 days ahead of imaging. We used 910nm wavelength (UltraII, Coherent) as
544 excitation light for all samples. Signals in the green and red spectrum were simultaneously
545 collected using 560 nm dichroic mirror at x,y = 1,1 μ m resolution in every 50 μ m z (for pericyte
546 mapping) or x,y,z = 1,1,5 μ m resolution (for vascular mapping).

547 We utilized our previously described software pipeline to perform de-aberration,
548 normalization, and imaging stitching steps for all STPT data collected for this study²⁸. Moreover,

549 we used the same analytical tools to binarize the vessel signals and skeletonize for further
550 analysis. This pipeline also performs cleaning/reconnecting of artifacts, traces the vessel
551 diameter, and finally outputs the coordinates for each vessel segment and its connectivity. For
552 pericyte cell counting, we used previously developed Deep Learning Neural Network (DLNN)
553 cell counting²⁸. This DLNN uses a per-cell multi-resolution-hybrid ResNet classification with
554 potential cell locations to reduce computational time and resources without loss of quality. While
555 aged mouse brains do have increased noise due to the accumulation of cellular debris, we
556 validated that our DLNN pipeline performed at the same level as with young adult mice and did
557 not incorporate cellular debris as potential cells.

558
559 **Tissue clearing, 3D immunolabeling, and LSFM imaging**
560 Whole brain vascular staining was performed following the iDISCO+ protocol with
561 modifications²⁴. Brain samples were delipidated in SBiP buffer, consisting of ice-cold water,
562 50mM Na₂HPO₄, 4% SDS, 2-methyl-2-butanol and 2-propanol. This buffer is activated at room
563 temperature and is therefore made and stored at 4°C before use. Each sample was submerged in
564 10ml of SBiP buffer, rotated at room temperature with buffer changes at 3 hours, 6 hours and
565 then incubated with fresh SBiP buffer overnight. For adequate delipidation, particularly for aged
566 samples, each brain was then washed with SBiP for a total of 6 days, with daily buffer changes.
567 After delipidation, brain samples were washed with B1n buffer, which consists of 0.1% TritonX-
568 100, 1g of glycine, 0.01% 10N NaOH and 20% NaN₃. Brain samples were washed with 10ml of
569 B1n buffer at room temperature for 2 days. To begin immunolabeling, brains were rinsed 3 times
570 for 1 hour each with PTwH buffer, consisting of 1X PBS, 0.2% Tween-20, 10mg heparin, and 2g
571 of NaN₃. For primary antibody incubations, antibodies were diluted in antibody solution
572 consisting of PTwH buffer with 5% DMSO and 3% normal donkey serum. Antibodies to smooth
573 muscle actin (Acta2) (Rabbit anti-Acta2, Abcam, cat: ab5694, dilution 1:1000) and transgelin
574 (Sm22) (Rabbit anti-Sm22 Abcam, cat: ab14106, dilution 1:1500) were combined to label the
575 artery wall, as previously described²⁴. Pan-vascular labeling was achieved through staining with
576 DyLight-594 labeled Lycopersicon Esculentum (Tomato) Lectin (Vector labs, cat. no.: DL-1177-
577 1), which was added to both primary and secondary incubations at 1:100 concentration. Pericytes
578 were labeled by combining PDGFR β (Goat anti- PDGFR β , R&D Systems, cat. no.: AF1042,
579 dilution: 1:100) and Mouse Aminopeptidase N/CD13 (Goat anti-CD13, R&D Systems, cat. no.:
580 AF2335, dilution: 1:100). Primary antibodies were incubated for 10 days at 37°C. Following
581 primary incubation, PTwH buffer was changed 4-5 times for each sample over the course of 24
582 hours. A fresh antibody solution was used to dilute all secondary antibodies to a concentration of
583 1:500. For secondary antibodies, Alexa Fluor® 488-AffiniPure Fab Fragment Donkey Anti-
584 Rabbit IgG (H+L) (Jackson ImmunoResearch laboratories, cat. no.: 711-547-003) was used to
585 detect artery staining and Alexa Fluor® 647-AffiniPure Fab Fragment Donkey Anti-Goat IgG
586 (H+L)
587 (Jackson ImmunoResearch laboratories, cat. no.: 705-607-003) was utilized to detect pericyte
588 staining. After secondary incubation for 10 days at 37°C, brains were washed 4-5 times in PTwH
589 buffer for 24 hours. Brain samples were then dehydrated in a series of methanol dilutions in
590 water (1-hour washes in 20%, 40%, 60%, 80% and 100%). An additional wash of 100%
591 methanol was conducted overnight to remove any remaining water. The next day, brains were
592 incubated in 66% dichloromethane/33% methanol for 3 hours and subsequently incubated in 100%
593 dichloromethane twice for at least 15 minutes each. Brains were equilibrated in dibenzyl ether
594 for at least two days before transitioning to ethyl cinnamate one day prior to imaging.

595 We used the SmartSPIM light sheet fluorescence microscope (LifeCanvas Technologies).
596 Brains were supported in the custom sample holder by standardized pieces of dehydrated agarose
597 consisting of 1% agarose in 1X TAE buffer. The sample holder arm was then submerged in ethyl
598 cinnamate for imaging. We used a 3.6X objective (LifeCanvas, 0.2NA, 12mm working distance,
599 1.8 μ m lateral resolution) and three lasers (488nm, 560nm, 642nm wavelengths) with a 2mm step
600 size. For detailed examination of pericytes, we used a 15X objective (Applied Scientific
601 Instrumentation, 0.4NA, 12mm working distance, 0.4mm lateral resolution) with a 1 μ m z step
602 size. Acquired data was stitched using custom Matlab codes adapted from Wobbly Stitcher²⁴.
603

604 **Analysis of LSFM-based vascular and pericyte signals**

605 For pericyte counting, prior to quantification, each stitched image stack, per signal channel, was
606 separately normalized, and the entire volume of each image stack was then converted to 20 μ m
607 maximum intensity projections (MIP). Normalization of each signal channel is done by adjusting
608 according to the histogram-determined global mean value of the background by utilizing a 10x
609 downsized copy of the entire image stack. The 20 μ m MIP step was determined to prevent over or
610 under counting of cell bodies, since pericyte cell body size tended to range from 6-10 μ m
611 depending on the orientation of the cell measured within a 3D context in the original image stack.
612 Finally, all three image channels (artery, lectin, and mural cell labels) were merged into a
613 channel overlay to provide additional context, such as vascular zone information. Cells with
614 stereotypical pericyte morphology (i.e., ovoid shape and protruding from the vessel wall),
615 typically along the first through third order arteriolar branches, that also expressed smooth
616 muscle markers and extended processes that wrapped around the vessel were classified as
617 ensheathing pericytes. Capillary pericytes were classified according to cell body shape and
618 localized to the capillary bed without any Acta2/Transgelin expression. These cells were further
619 subdivided into mesh or thin strand morphologies according to their microvessel placement and
620 type of processes, according to the definitions of these subtypes¹⁰⁵. Cell bodies along larger
621 veins, including the principle cortical venules were excluded from this analysis.

622 For arteriole analysis, 600 μ m MIPs were obtained from the channel labeling of Acta2
623 and Transgelin (i.e., artery labeling). We cropped the supplementary somatosensory cortex from
624 full datasets and quantified the total number of arteries and their branches manually.

625 For tortuosity measurements, a centerline of the entire vessel length was first traced to
626 obtain the Euclidean distance (arc length) using a skeletonization tool in Clearmap 2.0²⁴. Then a
627 straight line connecting the start and end points of the previous length was obtained to measure
628 the chord length. The arc chord ratio was then determined by dividing the Euclidean distance by
629 the arc chord distance. We used 32 arteries from 2-month-old (n=3 animals) and 23 from 24-
630 month-old (n=3 animals) in the medial prefrontal, and 19 arteries from 2-month-old (n=2
631 animals) and 23 from 24-month-old (n=3 animals). For Circle of Willis analysis, entire brain
632 datasets for the artery channel were converted to 10 μ m isotropic. Next, a cropped volume
633 including the branching point of the middle cerebral artery as well as ample segments of the
634 anterior communicating artery and middle cerebral artery were obtained within 250x250x120 μ m
635 (x,y,z) to fully capture the entire branch point and associated arteries in x,y,z dimensions. This
636 subset was re-sliced to obtain the cross-sectional area of this section of the vessel. The average
637 radius was obtained from the cross-sectional areas.
638

639 **Surgery, habituation, and measurement for *in vivo* recording**

640 Cerebral oxygenation, cerebral blood volume (CVB) and vessel diameter data were acquired
641 from the same groups of awake, behaving mice during voluntary locomotion and whisker
642 stimulation. All surgeries were performed under isoflurane anesthesia (in oxygen, 5% for
643 induction and 1.5-2% for maintenance). A custom-machined titanium head bolt was attached to
644 the skull with cyanoacrylate glue (#32002, Vibra-tite). The head bolt was positioned along the
645 midline and just posterior to the lambda cranial suture. Two self-tapping 3/32" #000 screws (J.I.
646 Morris) were implanted into the skull contralateral to the measurement sites over the frontal lobe
647 and parietal lobe. For measurements using two-photon laser scanning microscopy (2PLSM),
648 CBV measurement using intrinsic optical signal (IOS) imaging or brain oxygenation
649 measurement using spectroscopy, a polished and reinforced thin-skull (PoRTS) window was
650 made covering the right hemisphere or both hemispheres as described previously^{53-58,62}.
651 Following the surgery, mice were then returned to their home cage for recovery for at least one
652 week, and then started habituation on experimental apparatus. Habituation sessions were
653 performed 2-4 times per day over the course of one week, with the duration increasing from 5
654 min to 45 min.

655 Habituation. Animals were gradually acclimated to head-fixation on a spherical treadmill
656^{53,55,57,106} with one degree of freedom over at least three habituation sessions. The spherical
657 treadmill was covered with nonabrasive anti-slip tape (McMaster-Carr) and attached to an optical
658 rotary encoder (#E7PD-720-118, US Digital) to monitor locomotion. Mice were acclimated to
659 head-fixation for ~15 minutes during the first session and were head-fixed for longer durations
660 (> 1 hour) in the subsequent sessions. Mice were monitored for any signs of stress during
661 habituation. In all cases, the mice exhibited normal behaviors such as exploratory whisking and
662 occasional grooming after being head-fixed. Heart rate fluctuations were detectable in the
663 intrinsic optical signal^{53,62} and varied between 7 and 13 Hz for all mice after habituation, which
664 is comparable to the mean heart rate (~12 Hz) recorded telemetrically from mice in their home
665 cage¹⁰⁷. Habituation sessions were achieved 2-4 times per day over the course of one week, with
666 the duration increasing from 5 min to 45 min. Mice that received whisker stimulation (n = 10)
667 were acclimatized to head-fixation for 15–30 min during the first session. In subsequent sessions,
668 they began to receive air puffs directed at the whiskers and were head-fixed for longer durations
669 (> 60 minutes).

670 Physiological measurements. Data from all experiments (except two photon laser
671 scanning microscopy) were collected using custom software written in LabVIEW (version 2014,
672 National Instruments). *Behavioral measurement.* The treadmill movements were used to quantify
673 the locomotion events of the mouse. The animal was also monitored using a webcam (Microsoft
674 LifeCam Cinema®) as an additional behavioral measurement. *Vibrissa stimulation.* Animals
675 were awake and engaged in whisking behavior during IOS data acquisition^{54,56}. Brief (0.1-s
676 duration) puffs of air were delivered to the ipsilateral and contralateral whiskers through a thin
677 plastic tube (length 130 mm, diameter 2 mm). Air puffs were directed to the distal ends of the
678 whiskers at an angle parallel to the face to prevent stimulation of other parts of the head or face.
679 An additional air puffer was set up to point away from the body for use as an auditory stimulus.
680 The puffs were delivered via solenoid actuator valves (Sizto Tech Corporation, 2V025 1/4) at
681 constant air pressure (10 psi) maintained by an upstream regulator (Wilkerson, R03-02-000). Air
682 puffs were separated by intervals of 30-60 s, and the order of all sensory stimulation was
683 randomized, with a nominal ratio of three contralateral stimuli for every ipsilateral or auditory
684 stimulation. Auditory and ipsilateral stimuli were omitted from the principal analysis because
685 their responses were primarily related to stimulus-provoked movement. *Brain oxygen*

686 *measurement using optical imaging.* We mapped the spatiotemporal dynamics of oxyhemoglobin
687 and deoxyhemoglobin concentrations using their oxygen-dependent optical absorption spectra⁷².
688 Reflectance images were collected during periods of green LED light illumination at 530 nm
689 (equally absorbed by oxygenated and deoxygenated hemoglobin, M530L3, Thorlabs) or blue
690 LED light illumination at 470 nm (absorbed more by oxygenated than deoxygenated hemoglobin,
691 M470L3, Thorlabs). For these experiments, a CCD camera (Dalsa 1M60) was operated at 60 Hz
692 with 4X4 binning (256 X 256 pixels), mounted with a VZM300i optical zoom lens (Edmund
693 Optics). Green and blue reflectance data were converted to changes in oxy- and
694 deoxyhemoglobin concentrations using the modified Beer-Lambert law with Monte Carlo-
695 derived wavelength-dependent path length factors⁶¹. We used the cerebral oxygenation index⁷¹
696 (i.e., HbO-HbR) to quantify the change in oxygenation, as calculating the percentage change
697 requires knowledge of the concentration of hemoglobin on a pixel-by-pixel basis, which is not
698 feasible given the wide heterogeneity in the density of the cortical vasculature³⁰. *Measurements*
699 *using two-photon laser scanning microscopy (2PLSM).* Mice were briefly anesthetized with
700 isoflurane (5% in oxygen) and retro-orbitally injected with 50 μ L 5% (weight/volume in saline)
701 fluorescein-conjugated dextran (70 kDa, Sigma-Aldrich), and then fixed on a spherical treadmill.
702 Imaging was done on a Sutter Movable Objective Microscope with a 20X, 1.0 NA water dipping
703 objective (Olympus, XLUMPlanFLN). A MaiTai HP (Spectra-Physics, Santa Clara, CA) laser
704 tuned to 800 nm was used for fluorophore excitation. All imaging with the water-immersion lens
705 was done with room temperature distilled water. All the 2PLSM measurements were started at
706 least 20 minutes after isoflurane exposure to avoid the disruption of physiological signals due to
707 anesthetics.

708 For navigational purposes, wide field images were collected to generate vascular maps of
709 brain pial vascular maps of the entire PoRTS window. We performed three different
710 measurements using 2PLSM. (1) To measure blood vessel diameter responses to locomotion,
711 individual arteries and veins were imaged at nominal frame rate of 3 Hz for 5 minutes using 10-
712 15 mW of power exiting the objective. Diameter of pial vessels were calculated using Radon
713 transform¹⁰⁸. (2) To measure RBC velocity and RBC spacing, line scan images were collected
714 from individual capillaries (diameter range: 2-8 μ m). The pixel dwell time for the line scan
715 segments was 1 μ s and we achieved a \sim 1.5 kHz sampling rate. (3) To measure the vasculature
716 diameter under physiological conditions (i.e., awake and resting), we collected stack image every
717 other day for each mouse. For each mouse, we collected data from 4 different days and collected
718 3 different trials on each day. Shortly (within 20 minutes) after the last trial on the last day, the
719 mouse was perfused for future vasculature reconstruction. The resolution for each XY plane is
720 0.64 μ m/pixel and the resolution for Z direction is 1 μ m. On the Z-direction, three frames were
721 collected and averaged, the averaged frame was saved in the file. All the images were acquired
722 with increasing laser power up to 100 mW at a depth of \sim 200 μ m.

723 *Isoflurane challenge.* To compare the capability of vasodilation in both young and aged
724 mice, we exposed a subset of mice to short period (\sim 2 minutes) of isoflurane (5% in pure
725 oxygen) and imaged the pial vessel (specifically, the branch of the middle cerebral artery)
726 diameter responses. This allowed us to assess the magnitude of diameter change of pial arteries
727 and veins.

728 *Oxygen challenge experiments.* In a subset of experiments, hyperoxia was induced by
729 substituting breathing air for 100% pure oxygen. Using optical imaging of spectroscopy, we
730 performed an oxygen challenge. Mice were head-fixed on a spherical treadmill, and a nose cone
731 was fixed \sim 1 inch in front of the nose, with care taken not to contact the whiskers. Two gases

732 were administered during a 5-min spectroscopy trial in the following order: 1 min breathable air
 733 (21% oxygen), 3 min 100% oxygen, and 1 min breathable air. Mice breathed breathable air for at
 734 least 2 min between trials, to ensure physiological parameters returned to baseline. Reflectance
 735 images were collected during periods of green LED light illumination at 530 nm (equally
 736 absorbed by oxygenated and deoxygenated hemoglobin, M530L3, Thorlabs) or blue LED light
 737 illumination at 470 nm (absorbed more by oxygenated than deoxygenated hemoglobin, M470L3,
 738 Thorlabs) or red LED light illumination at 660 nm (absorbed more by deoxygenated than
 739 oxygenated hemoglobin, M660L2, Thorlabs).

740

741 **Data analysis for *in vivo* recording.**

742 All data analyses were performed in Matlab (R2019b, MathWorks) using custom code.

743 *Locomotion event identification.* Locomotion events^{53,57,106} from the spherical treadmill were
 744 identified by first applying a low-pass filter (10 Hz, 5th order Butterworth) to the velocity signal
 745 from the optical rotary encoder, and then comparing the absolute value of acceleration (first
 746 derivative of the velocity signal) to a threshold of 3 cm/s². Periods of locomotion were
 747 categorized based on the binarized detection of the treadmill acceleration:

$$\delta(t) = \theta(|a_t| - a_c) = \begin{cases} 1, & |a_t| \geq a_c \\ 0, & |a_t| < a_c \end{cases}$$

748 where a_t is the acceleration at time t , and a_c is the treadmill acceleration threshold.

749 *Spontaneous activity.* To characterize spontaneous (non-locomotion-evoked) activity, we defined
 750 “resting” periods as periods started 4 seconds after the end of previous locomotion event and
 751 lasting no less than 60 seconds.

752 *Calculation of hemodynamic response function.* We considered the neurovascular relationship to
 753 be a linear time invariant system^{69,109,110}. To provide a model-free approach to assess the
 754 relationship between CBV or vessel diameter and neural activity, hemodynamic response
 755 function (HRF) was calculated by deconvoluting CBV signal, oxygen signal or vessel diameter
 756 signal to locomotion events, respectively, using the following equation:

$$H_{(k+1) \times 1} = (L^T L)^{-1} L^T V_{(m+k) \times 1}$$

757 H is the HRF, V is the tissue oxygenation signal or neural activity signal. L is a Toeplitz matrix
 758 of size $(m+k) \times (k+1)$ containing binarized locomotion events (n):

$$L(\vec{n}) = \begin{pmatrix} 1 & n_1 & 0 & 0 & \dots & 0 \\ 1 & n_2 & n_1 & 0 & \dots & 0 \\ \vdots & \vdots & n_2 & n_1 & \dots & \vdots \\ \vdots & n_k & \vdots & n_2 & \dots & n_1 \\ \vdots & 0 & n_k & \vdots & \dots & n_2 \\ \vdots & \vdots & \vdots & n_k & \ddots & \vdots \\ 1 & 0 & 0 & 0 & \dots & n_k \end{pmatrix}$$

759 *Comparison of HRF parameters.* To quantify the temporal features of HRF, the HRF for CBV
 760 was fitted using a gamma-variate fitting process^{69,111–114} using a gamma-variate function kernel
 761 of the following form,

$$762 \text{HRF}(t, T, W, A) = A * \left(\frac{t}{T}\right)^\alpha * e^{\left(\frac{t-T}{-\beta}\right)},$$

763 where $\alpha = (T/W)^2 * 8.0 * \log(2.0)$, $\beta = W^2 / (T * 8.0 * \log(2.0))$. For modeling HRF using a
 764 gamma-variate function kernel, we used a downhill simplex algorithm minimizing the sum
 765 square difference between measured and predicted hemodynamics. The goodness of fit was

766 quantified as $R^2 = 1 - \frac{\sum(HRF_{actual} - HRF_{model})^2}{\sum(HRF_{actual} - \overline{HRF})^2}$, where \overline{HRF} is the mean value of the actual HRF.

767 To quantify the amplitude of each HRF, we used the value at the peak of the modeled HRF.
768 Time to peak (TTP) was calculated as the time at which the modeled HRF reached its maximum
769 amplitude. Full-width at half maximum (FWHM) was defined as the time from which the
770 modeled HRF rose to 50% of its peak until it fell to 50% of its peak. TTP, FWHM and HRF
771 amplitudes across different cortical depths were compared using a linear model to quantify
772 trends (robustfit, MATLAB).

773 *2PLSM image processing.* (1) To quantify blood vessel diameter responses to locomotion,
774 individual frames from 2PLSM imaging were aligned using a rigid registration algorithm to
775 remove motion artifacts in the x–y plane⁵⁹. Visual inspection of movies indicated that there was
776 minimal z-axis motion. A rectangular box was manually drawn around a short segment of the
777 vessel and the pixel intensity was averaged along the long axis⁵⁹. Pixel intensity was used to
778 calculate diameter from the full-width at half-maximum. Periods of rest were segregated using
779 locomotion events measured with the rotary encoder. For each 5-min trial, diameter
780 measurements were normalized to the average diameter during periods of rest. The diameters
781 were smoothed with a third-order, 15-point Savitzky–Golay filter (Matlab function: `sgolayfilt`).
782 (2) To quantify RBC velocity, blood flow velocity was calculated using Radon transform⁵⁸.
783 Only blood flow velocity during resting periods was reported. Capillary diameter was manually
784 measured using ImageJ software. To quantify RBC spacing, we utilized the method reported in
785 our previous study⁵⁵. We identified RBC “stall” events as an inter-RBC spacing greater than 1
786 second. We only used RBCs spacing intervals during relatively long resting segments (i.e., ≥ 5
787 second). (3) As the perfusion procedure and brain fixation might affect the brain vasculature¹¹⁵,
788 to compare our measurements for vessel radii in STPT and LSFM imaging datasets to vessel
789 parameters measured in vivo using 2PLSM, the same animals that were used for 2PLSM and
790 STPT imaging were reconstructed and compared, as described before²⁸.

791 792 **Statistical analysis**

793 For the STPT and LSFM dataset, we used Matlab (Mathworks) and/or Prism (Graphpad) for all
794 statistical analysis, including multi-region of interest (ROI) correlation analysis. We used an
795 averaged value of the experimented animals while treating each ROI as an individual data point.
796 For two group comparisons, multiple unpaired t-tests were used with multiple comparison
797 corrections. The p value was adjusted with the false discovery rate for multiple comparison
798 corrections using the Two-stage step-up method of Benjamini, Krieger and Yekutieli in
799 Graphpad. For multiple group comparisons, two-way ANOVA, or mixed model if including
800 NaN values, to generate comparison between groups using Prism (Graphpad).
801 For *in vivo* recording, all summary data were reported as the mean \pm standard deviation (SD)
802 unless stated otherwise. The normality of the samples was tested before statistical testing using
803 the Anderson-Darling test (`adtest`). For comparison of multiple populations, the assumption of
804 equal variance for parametric statistical method was also tested (`vartest2`). If criteria of normality
805 and equal variance were not met, parametric tests (unpaired t test) were replaced with a
806 nonparametric method (Wilcoxon rank sum test). For comparisons of oxygen challenge and
807 isoflurane challenge effects on brain hemodynamics across different age groups, we used the
808 linear mixed effect model (MATLAB function: `fitlme`). Significance was accepted at $p < 0.05$.

809 **References**

- 810 1. Lu, H. *et al.* Alterations in cerebral metabolic rate and blood supply across the adult lifespan.
811 *Cereb Cortex* **21**, 1426–1434 (2011).
- 812 2. Pfister, F. *et al.* Pericyte migration: A novel mechanism of pericyte loss in experimental
813 diabetic retinopathy. *Diabetes* (2008) doi:10.2337/db08-0325.
- 814 3. Brown, W. R. & Thore, C. R. Review: Cerebral microvascular pathology in ageing and
815 neurodegeneration. *Neuropathology and Applied Neurobiology* **37**, 56–74 (2011).
- 816 4. Baloyannis, S. J. & Baloyannis, I. S. The vascular factor in Alzheimer’s disease: A study in
817 Golgi technique and electron microscopy. *Journal of the Neurological Sciences* **322**, 117–
818 121 (2012).
- 819 5. Almeida, V. M. *et al.* Pericytes Make Spinal Cord Breathless after Injury. *Neuroscientist* **24**,
820 440–447 (2018).
- 821 6. Hayden. Type 2 Diabetes Mellitus Increases The Risk of Late-Onset Alzheimer’s Disease:
822 Ultrastructural Remodeling of the Neurovascular Unit and Diabetic Gliopathy. *Brain*
823 *Sciences* **9**, 262 (2019).
- 824 7. Abrahamson, E. E. & Ikonovic, M. D. Brain injury-induced dysfunction of the blood brain
825 barrier as a risk for dementia. *Experimental Neurology* **328**, 113257 (2020).
- 826 8. Uemura, M. T., Maki, T., Ihara, M., Lee, V. M. Y. & Trojanowski, J. Q. Brain Microvascular
827 Pericytes in Vascular Cognitive Impairment and Dementia. *Front. Aging Neurosci.* **12**, 80
828 (2020).
- 829 9. Iadecola, C. *et al.* The Neurovasculome: Key Roles in Brain Health and Cognitive Impairment:
830 A Scientific Statement From the American Heart Association/American Stroke Association.
831 *Stroke* **0**, (2023).

- 832 10. Kapogiannis, D. & Mattson, M. P. Disrupted energy metabolism and neuronal circuit
833 dysfunction in cognitive impairment and Alzheimer's disease. *Lancet Neurol* **10**, 187–198
834 (2011).
- 835 11. Cunnane, S. C. *et al.* Brain energy rescue: an emerging therapeutic concept for
836 neurodegenerative disorders of ageing. *Nat Rev Drug Discov* **19**, 609–633 (2020).
- 837 12. Nedergaard, M. & Goldman, S. A. Glymphatic failure as a final common pathway to
838 dementia. *Science* **370**, 50–56 (2020).
- 839 13. Hartmann, D. A., Coelho-Santos, V. & Shih, A. Y. Pericyte Control of Blood Flow Across
840 Microvascular Zones in the Central Nervous System. *Annu Rev Physiol* **84**, 331–354 (2022).
- 841 14. Sweeney, M. D., Zhao, Z., Montagne, A., Nelson, A. R. & Zlokovic, B. V. Blood-Brain
842 Barrier: From Physiology to Disease and Back. *Physiological reviews* **99**, 21–78 (2019).
- 843 15. Hartmann, D. A. *et al.* Brain capillary pericytes exert a substantial but slow influence on
844 blood flow. *Nature Neuroscience* **24**, 633–645 (2021).
- 845 16. Yang, T., Sun, Y., Lu, Z., Leak, R. K. & Zhang, F. The impact of cerebrovascular aging on
846 vascular cognitive impairment and dementia. *Ageing Res Rev* **34**, 15–29 (2017).
- 847 17. *Pericyte Biology in Disease*. vol. 1147 (Springer International Publishing, 2019).
- 848 18. Ding, R. *et al.* Loss of capillary pericytes and the blood–brain barrier in white matter in
849 poststroke and vascular dementias and Alzheimer's disease. *Brain Pathol.* **30**, 1087–1101
850 (2020).
- 851 19. Li, Y. *et al.* Aging-associated changes in cerebral vasculature and blood flow as determined
852 by quantitative optical coherence tomography angiography. *Neurobiology of Aging* **70**,
853 148–159 (2018).

- 854 20. Tarumi, T. & Zhang, R. Cerebral Blood Flow in Normal Aging Adults: Cardiovascular
855 Determinants, Clinical Implications, and Aerobic Fitness. *J Neurochem* **144**, 595–608
856 (2018).
- 857 21. Juttukonda, M. R. *et al.* Characterizing cerebral hemodynamics across the adult lifespan with
858 arterial spin labeling MRI data from the Human Connectome Project-Aging. *Neuroimage*
859 **230**, 117807 (2021).
- 860 22. Sweeney, M. D., Kisler, K., Montagne, A., Toga, A. W. & Zlokovic, B. V. The role of brain
861 vasculature in neurodegenerative disorders. *Nature Neuroscience* **21**, 1318–1331 (2018).
- 862 23. Xiong, B. *et al.* Precise Cerebral Vascular Atlas in Stereotaxic Coordinates of Whole Mouse
863 Brain. *Frontiers in Neuroanatomy* **11**, 128 (2017).
- 864 24. Kirst, C. *et al.* Mapping the Fine-Scale Organization and Plasticity of the Brain Vasculature
865 Resource Mapping the Fine-Scale Organization and Plasticity of the Brain Vasculature.
866 *Cell* 1–16 (2020) doi:10.1016/j.cell.2020.01.028.
- 867 25. Todorov, M. I. *et al.* Machine learning analysis of whole mouse brain vasculature. *Nature*
868 *Methods* **17**, 442–449 (2020).
- 869 26. Ji, X. *et al.* Brain microvasculature has a common topology with local differences in
870 geometry that match metabolic load. *Neuron* **109**, 1168-1187.e13 (2021).
- 871 27. Bennett, H. C. & Kim, Y. Advances in studying whole mouse brain vasculature using high-
872 resolution 3D light microscopy imaging. *NPh* **9**, 021902 (2022).
- 873 28. Wu, Y. *et al.* Quantitative relationship between cerebrovascular network and neuronal cell
874 types in mice. *Cell Reports* **39**, (2022).
- 875 29. Blinder, P. *et al.* The cortical angiome: an interconnected vascular network with
876 noncolumnar patterns of blood flow. *Nat Neurosci* **16**, 889–897 (2013).

- 877 30. Tsai, P. S. *et al.* Correlations of Neuronal and Microvascular Densities in Murine Cortex
878 Revealed by Direct Counting and Colocalization of Nuclei and Vessels. *Journal of*
879 *Neuroscience* **29**, 14553–14570 (2009).
- 880 31. Liwang, J. K., Bennett, H. C., Pi, H.-J. & Kim, Y. Protocol for using serial two-photon
881 tomography to map cell types and cerebrovasculature at single-cell resolution in the whole
882 adult mouse brain. *STAR Protoc* **4**, 102048 (2023).
- 883 32. Wang, Q. *et al.* The Allen Mouse Brain Common Coordinate Framework: A 3D Reference
884 Atlas. *Cell* **181**, 936-953.e20 (2020).
- 885 33. Maheswaran, S. *et al.* Longitudinal regional brain volume changes quantified in normal
886 aging and Alzheimer’s APP x PS1 mice using MRI. *Brain Res* **1270**, 19–32 (2009).
- 887 34. Berthiaume, A.-A. *et al.* Pericyte remodeling is deficient in the aged brain and contributes to
888 impaired capillary flow and structure. *Nat Commun* **13**, 5912 (2022).
- 889 35. Brown, L. S. *et al.* Pericytes and Neurovascular Function in the Healthy and Diseased Brain.
890 *Front. Cell. Neurosci.* **13**, 282 (2019).
- 891 36. Berthiaume, A. A. *et al.* Dynamic Remodeling of Pericytes In Vivo Maintains Capillary
892 Coverage in the Adult Mouse Brain. *Cell Reports* **22**, 8–16 (2018).
- 893 37. Cuttler, A. S. *et al.* Characterization of Pdgfrb-Cre transgenic mice reveals reduction of
894 ROSA26 reporter activity in remodeling arteries. *Genesis (New York, N.Y. □: 2000)* **49**,
895 673–680 (2011).
- 896 38. Hartmann, D. A., Underly, R. G., Watson, A. N. & Shih, A. Y. A murine toolbox for
897 imaging the neurovascular unit. *Microcirculation (New York, N.Y. □: 1994)* **22**, 168–182
898 (2015).

- 899 39. Alheid, G. F. Extended amygdala and basal forebrain. *Ann N Y Acad Sci* **985**, 185–205
900 (2003).
- 901 40. Sato, A., Sato, Y. & Uchida, S. Regulation of cerebral cortical blood flow by the basal
902 forebrain cholinergic fibers and aging. *Autonomic Neuroscience* **96**, 13–19 (2002).
- 903 41. Ballinger, E. C., Ananth, M., Talmage, D. A. & Role, L. W. Basal Forebrain Cholinergic
904 Circuits and Signaling in Cognition and Cognitive Decline. *Neuron* **91**, 1199–1218 (2016).
- 905 42. Zolnik, T. A. *et al.* Layer 6b Is Driven by Intracortical Long-Range Projection Neurons. *Cell*
906 *Reports* **30**, 3492-3505.e5 (2020).
- 907 43. Trache, A., Massett, M. P. & Woodman, C. R. Vascular smooth muscle stiffness and its role
908 in aging. in *Current Topics in Membranes* vol. 86 217–253 (Elsevier, 2020).
- 909 44. Montero, D., Pierce, G. L., Stehouwer, C. D. A., Padilla, J. & Thijssen, D. H. J. The impact
910 of age on vascular smooth muscle function in humans: *Journal of Hypertension* **33**, 445–
911 453 (2015).
- 912 45. Nishimura, N., Schaffer, C. B., Friedman, B., Lyden, P. D. & Kleinfeld, D. Penetrating
913 arterioles are a bottleneck in the perfusion of neocortex. *Proc Natl Acad Sci U S A* **104**,
914 365–370 (2007).
- 915 46. Shih, A. Y. *et al.* Robust and fragile aspects of cortical blood flow in relation to the
916 underlying angioarchitecture. *Microcirculation* **22**, 204–218 (2015).
- 917 47. Ciurică, S. *et al.* Arterial Tortuosity. *Hypertension* **73**, 951–960 (2019).
- 918 48. Weiss, D. *et al.* Mechanics-driven mechanobiological mechanisms of arterial tortuosity. *Sci*
919 *Adv* **6**, eabd3574 (2020).

- 920 49. Cai, C. *et al.* Impaired dynamics of precapillary sphincters and pericytes at first-order
921 capillaries predict reduced neurovascular function in the aging mouse brain. *Nat Aging* **3**,
922 173–184 (2023).
- 923 50. Khan, U. A. *et al.* Molecular drivers and cortical spread of lateral entorhinal cortex
924 dysfunction in preclinical Alzheimer’s disease. *Nat Neurosci* **17**, 304–311 (2014).
- 925 51. Van Hoesen, G. W., Hyman, B. T. & Damasio, A. R. Entorhinal cortex pathology in
926 Alzheimer’s disease. *Hippocampus* **1**, 1–8 (1991).
- 927 52. Rodriguez, G. A., Burns, M. P., Weeber, E. J. & Rebeck, G. W. Young APOE4 targeted
928 replacement mice exhibit poor spatial learning and memory, with reduced dendritic spine
929 density in the medial entorhinal cortex. *Learning & Memory* **20**, 256–266 (2013).
- 930 53. Zhang, Q. *et al.* Cerebral oxygenation during locomotion is modulated by respiration. *Nature*
931 *Communications* **10**, 1–15 (2019).
- 932 54. Winder, A. T., Echagarruga, C., Zhang, Q. & Drew, P. J. Weak correlations between
933 hemodynamic signals and ongoing neural activity during the resting state. *Nature*
934 *Neuroscience* **20**, 1761–1769 (2017).
- 935 55. Zhang, Q., Gheres, K. W. & Drew, P. J. Origins of 1/f-like tissue oxygenation fluctuations in
936 the murine cortex. *PLOS Biology* **19**, (2021).
- 937 56. Zhang, Q., Turner, K. L., Gheres, K. W., Hossain, M. S. & Drew, P. J. Behavioral and
938 physiological monitoring for awake neurovascular coupling experiments: a how-to guide.
939 *Neurophotonics* **9**, (2022).
- 940 57. Huo, B.-X., Smith, J. B. & Drew, P. J. Neurovascular coupling and decoupling in the cortex
941 during voluntary locomotion. *Journal of Neuroscience* **34**, 10975–10981 (2014).

- 942 58. Drew, P. J. *et al.* Chronic optical access through a polished and reinforced thinned skull. *Nat*
943 *Methods* **7**, 981–984 (2010).
- 944 59. Drew, P. J., Shih, A. Y. & Kleinfeld, D. Fluctuating and sensory-induced vasodynamics in
945 rodent cortex extend arteriole capacity. *Proc Natl Acad Sci U S A* **108**, 8473–8 (2011).
- 946 60. Hillman, E. M. Coupling mechanism and significance of the BOLD signal: a status report.
947 *Annu Rev Neurosci* **37**, 161–81 (2014).
- 948 61. Ma, Y. *et al.* Wide-field optical mapping of neural activity and brain haemodynamics:
949 considerations and novel approaches. *Philos Trans R Soc Lond B Biol Sci* **371**, (2016).
- 950 62. Huo, B. X., Gao, Y. R. & Drew, P. J. Quantitative separation of arterial and venous cerebral
951 blood volume increases during voluntary locomotion. *Neuroimage* **105**, 369–79 (2015).
- 952 63. Vazquez, A. L., Fukuda, M., Crowley, J. C. & Kim, S.-G. Neural and Hemodynamic
953 Responses Elicited by Forelimb- and Photo-stimulation in Channelrhodopsin-2 Mice:
954 Insights into the Hemodynamic Point Spread Function. *Cerebral cortex (New York, N.Y. □:*
955 *1991)* **24**, 2908–2919 (2014).
- 956 64. Tian, P. *et al.* Cortical depth-specific microvascular dilation underlies laminar differences in
957 blood oxygenation level-dependent functional MRI signal. *Proc Natl Acad Sci U S A* **107**,
958 15246–51 (2010).
- 959 65. Longden, T. A. *et al.* Capillary K⁺-sensing initiates retrograde hyperpolarization to increase
960 local cerebral blood flow. *Nat Neurosci* **20**, 717–726 (2017).
- 961 66. Rungta, R. L., Chaigneau, E., Osmanski, B.-F. & Charpak, S. Vascular
962 Compartmentalization of Functional Hyperemia from the Synapse to the Pia. *Neuron* **99**,
963 362-375.e4 (2018).

- 964 67. Rungta, R. L. *et al.* Diversity of neurovascular coupling dynamics along vascular arbors in
965 layer II/III somatosensory cortex. *Commun Biol* **4**, 855 (2021).
- 966 68. Bergel, A. *et al.* Adaptive modulation of brain hemodynamics across stereotyped running
967 episodes. *Nat Commun* **11**, 6193 (2020).
- 968 69. Cardoso, M. M., Sirotin, Y. B., Lima, B., Glushenkova, E. & Das, A. The neuroimaging
969 signal is a linear sum of neurally distinct stimulus- and task-related components. *Nat*
970 *Neurosci* **15**, 1298–306 (2012).
- 971 70. Drew, P. J. Vascular and neural basis of the BOLD signal. *Curr Opin Neurobiol* **58**, 61–69
972 (2019).
- 973 71. Boas, D. A. & Franceschini, M. A. Haemoglobin oxygen saturation as a biomarker: the
974 problem and a solution. *Philos Trans A Math Phys Eng Sci* **369**, 4407–24 (2011).
- 975 72. Lyons, D. G., Parpaleix, A., Roche, M. & Charpak, S. Mapping oxygen concentration in the
976 awake mouse brain. *Elife* **5**, (2016).
- 977 73. Pandya, V. A. & Patani, R. Region-specific vulnerability in neurodegeneration: lessons from
978 normal ageing. *Ageing Res Rev* **67**, 101311 (2021).
- 979 74. Erdő, F., Denes, L. & de Lange, E. Age-associated physiological and pathological changes at
980 the blood-brain barrier: A review. *J Cereb Blood Flow Metab* **37**, 4–24 (2017).
- 981 75. Zimmerman, B., Rypma, B., Gratton, G. & Fabiani, M. Age-related changes in
982 cerebrovascular health and their effects on neural function and cognition: A comprehensive
983 review. *Psychophysiology* **58**, e13796 (2021).
- 984 76. Lowerison, M. R. *et al.* Aging-related cerebral microvascular changes visualized using
985 ultrasound localization microscopy in the living mouse. *Sci Rep* **12**, 619 (2022).

- 986 77. Gunning-Dixon, F. M., Brickman, A. M., Cheng, J. C. & Alexopoulos, G. S. Aging of
987 Cerebral White Matter: A Review of MRI Findings. *Int J Geriatr Psychiatry* **24**, 109–117
988 (2009).
- 989 78. Fulop, G. A. *et al.* Role of age-related alterations of the cerebral venous circulation in the
990 pathogenesis of vascular cognitive impairment. *American Journal of Physiology-Heart and*
991 *Circulatory Physiology* **316**, H1124–H1140 (2019).
- 992 79. Sun, Z. *et al.* Age-Related Tortuosity of Carotid and Vertebral Arteries: Quantitative
993 Evaluation With MR Angiography. *Frontiers in Neurology* **13**, (2022).
- 994 80. Oliveros, E. *et al.* Hypertension in older adults: Assessment, management, and challenges.
995 *Clin Cardiol* **43**, 99–107 (2019).
- 996 81. Schager, B. & Brown, C. E. Susceptibility to capillary plugging can predict brain region
997 specific vessel loss with aging. *J Cereb Blood Flow Metab* **40**, 2475–2490 (2020).
- 998 82. Hoerder-Suabedissen, A. *et al.* Subset of Cortical Layer 6b Neurons Selectively Innervates
999 Higher Order Thalamic Nuclei in Mice. *Cereb Cortex* **28**, 1882–1897 (2018).
- 1000 83. Hoyer, D. & Jacobson, L. H. Orexin in sleep, addiction and more: Is the perfect insomnia
1001 drug at hand? *Neuropeptides* **47**, 477–488 (2013).
- 1002 84. Nixon, J. P. *et al.* Sleep disorders, obesity, and aging: the role of orexin. *Ageing Res Rev* **20**,
1003 63–73 (2015).
- 1004 85. Zaborszky, L. *et al.* Specific Basal Forebrain-Cortical Cholinergic Circuits Coordinate
1005 Cognitive Operations. *Journal of Neuroscience* **38**, 9446–9458 (2018).
- 1006 86. Li, X. *et al.* Generation of a whole-brain atlas for the cholinergic system and mesoscopic
1007 projectome analysis of basal forebrain cholinergic neurons. *Proceedings of the National*
1008 *Academy of Sciences* **115**, 415–420 (2018).

- 1009 87. Grothe, M. *et al.* Reduction of basal forebrain cholinergic system parallels cognitive
1010 impairment in patients at high risk of developing Alzheimer's disease. *Cerebral cortex*
1011 (*New York, NY*: 1991) **20**, 1685–1695 (2010).
- 1012 88. Fischer, V. W., Siddiqi, A. & Yusufaly, Y. Altered angioarchitecture in selected areas of
1013 brains with Alzheimer's disease. *Acta Neuropathol* **79**, 672–679 (1990).
- 1014 89. Casu, M. A., Pan Wong, T., De Koninck, Y., Ribeiro-da-Silva, A. & Cuello, A. C. Aging
1015 Causes a Preferential Loss of Cholinergic Innervation of Characterized Neocortical
1016 Pyramidal Neurons. *Cerebral Cortex* **12**, 329–337 (2002).
- 1017 90. Sagare, A. P. *et al.* Pericyte loss influences Alzheimer-like neurodegeneration in mice.
1018 *Nature Communications* **4**, (2013).
- 1019 91. Zhang, X. *et al.* High-resolution mapping of brain vasculature and its impairment in the
1020 hippocampus of Alzheimer's disease mice. *National Science Review* **6**, 1223–1238 (2019).
- 1021 92. Bekar, L. K., Wei, H. S. & Nedergaard, M. The locus coeruleus-norepinephrine network
1022 optimizes coupling of cerebral blood volume with oxygen demand. *J Cereb Blood Flow*
1023 *Metab* **32**, 2135–2145 (2012).
- 1024 93. Jacobs, H. I. L. *et al.* In vivo and neuropathology data support locus coeruleus integrity as
1025 indicator of Alzheimer's disease pathology and cognitive decline. *Sci Transl Med* **13**,
1026 eabj2511 (2021).
- 1027 94. Korkushko, O. V., Ivanov, L. A., Pizaruk, A. V. & Chebotarev, N. D. The respiratory
1028 function of blood in elderly and old age and the factors that determine it. *Human*
1029 *Physiology* **35**, 163–169 (2009).
- 1030 95. Moeini, M. *et al.* Compromised microvascular oxygen delivery increases brain tissue
1031 vulnerability with age. *Sci Rep-Uk* **8**, 8219 (2018).

- 1032 96. Haas, C. F., Loik, P. S. & Gay, S. E. Airway clearance applications in the elderly and in
1033 patients with neurologic or neuromuscular compromise. *Respir Care* **52**, 1362–81;
1034 discussion 1381 (2007).
- 1035 97. Schulte, H., Muhlfeld, C. & Brandenberger, C. Age-Related Structural and Functional
1036 Changes in the Mouse Lung. *Front Physiol* **10**, 1466 (2019).
- 1037 98. Haberman, R. P., Koh, M. T. & Gallagher, M. Heightened cortical excitability in aged
1038 rodents with memory impairment. *Neurobiol Aging* **54**, 144–151 (2017).
- 1039 99. Fischer, C. *et al.* Prevention of age-associated neuronal hyperexcitability with improved
1040 learning and attention upon knockout or antagonism of LPAR2. *Cell Mol Life Sci* **78**, 1029–
1041 1050 (2021).
- 1042 100. Popescu, I. R. *et al.* Increased intrinsic excitability and decreased synaptic inhibition in
1043 aged somatosensory cortex pyramidal neurons. *Neurobiol Aging* **98**, 88–98 (2021).
- 1044 101. Kapasi, A. *et al.* Watershed Microinfarct Pathology and Cognition in Older Persons.
1045 *Neurobiol Aging* **70**, 10–17 (2018).
- 1046 102. Drew, P. J. Neurovascular coupling: motive unknown. *Trends Neurosci* **45**, 809–819 (2022).
- 1047 103. Wang, T. *et al.* Three-photon imaging of mouse brain structure and function through the
1048 intact skull. *Nat Methods* **15**, 789–792 (2018).
- 1049 104. Brunner, C. *et al.* Whole-brain functional ultrasound imaging in awake head-fixed mice.
1050 *Nat Protoc* **16**, 3547–3571 (2021).
- 1051 105. Grant, R. I. *et al.* Organizational hierarchy and structural diversity of microvascular
1052 pericytes in adult mouse cortex. *Journal of Cerebral Blood Flow and Metabolism* **39**, 411–
1053 425 (2019).

- 1054 106. Gao, Y. R. & Drew, P. J. Effects of Voluntary Locomotion and Calcitonin Gene-Related
1055 Peptide on the Dynamics of Single Dural Vessels in Awake Mice. *J Neurosci* **36**, 2503–16
1056 (2016).
- 1057 107. Gehrman, J. *et al.* Phenotypic screening for heart rate variability in the mouse. *Am J*
1058 *Physiol Heart Circ Physiol* **279**, H733-40 (2000).
- 1059 108. Drew, P. J., Blinder, P., Cauwenberghs, G., Shih, A. Y. & Kleinfeld, D. Rapid
1060 determination of particle velocity from space-time images using the Radon transform. *J*
1061 *Comput Neurosci* **29**, 5–11 (2010).
- 1062 109. Boynton, G. M., Engel, S. A., Glover, G. H. & Heeger, D. J. Linear systems analysis of
1063 functional magnetic resonance imaging in human V1. *J Neurosci* **16**, 4207–21 (1996).
- 1064 110. Glover, G. H. Deconvolution of impulse response in event-related BOLD fMRI.
1065 *Neuroimage* **9**, 416–29 (1999).
- 1066 111. Madsen, M. T. A simplified formulation of the gamma variate function. *Phys Med Biol* **37**,
1067 1597–1600 (1992).
- 1068 112. Cohen, M. S. Parametric analysis of fMRI data using linear systems methods. *Neuroimage*
1069 **6**, 93–103 (1997).
- 1070 113. Sirotnin, Y. B. & Das, A. Anticipatory haemodynamic signals in sensory cortex not
1071 predicted by local neuronal activity. *Nature* **457**, 475–9 (2009).
- 1072 114. Yu, X., Qian, C., Chen, D. Y., Dodd, S. J. & Koretsky, A. P. Deciphering laminar-specific
1073 neural inputs with line-scanning fMRI. *Nat Methods* **11**, 55–8 (2014).
- 1074 115. Korogod, N., Petersen, C. C. & Knott, G. W. Ultrastructural analysis of adult mouse
1075 neocortex comparing aldehyde perfusion with cryo fixation. *Elife* **4**, (2015).
- 1076
1077

Figure 1

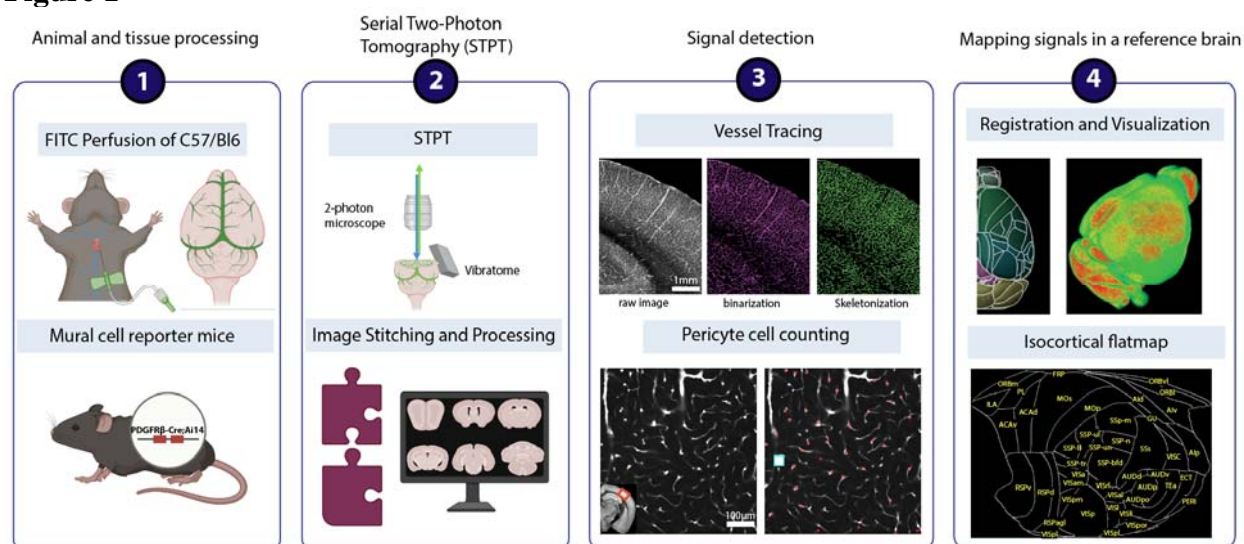


Figure 1. STPT based vessel tracing and pericyte counting pipeline

The steps of the STPT pipeline are outlined in order. **1.** Brain sample collection: vascular filling procedure via cardiac perfusion with FITC conjugated albumin gel and pericyte mapping using PDGFR β -Cre;Ai14 reporter mice. **2.** STPT imaging: combination of 2-photon microscope 2D tile imaging with serial vibratome sectioning to obtain cellular resolution images of the whole mouse brain. These image tiles are then stitched to reconstruct tissue sections spanning the olfactory bulb to the cerebellum. **3.** Signal detection: vascular tracing with binarization of FITC filled vascular signals and skeletonization, and deep learning-based detection of capillary pericytes. **4.** Mapping signals in a reference brain: All detected signals were registered to the Allen Common Coordinate Framework (Allen CCF) and an isocortical flatmap was used to examine signals in the isocortex.

Figure 2

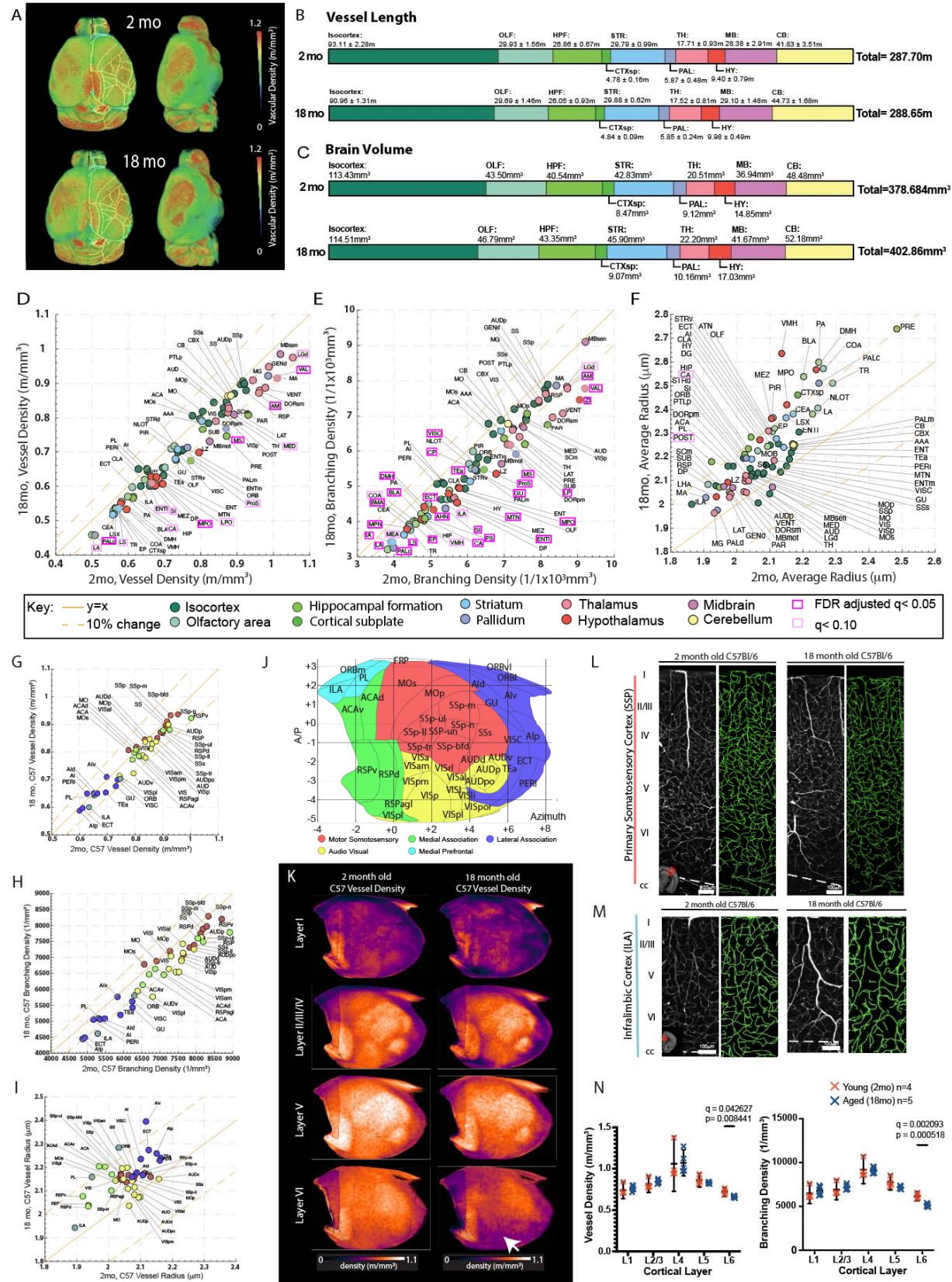


Figure 2. Region specific reduction of vascular length and branching density and increased vascular radii

(A) The averaged vasculature length density of 2-month-old (N=4) and 18-month-old (N=5) brains registered to the Allen CCF. (B-C) Summed vessel length (B) and brain volume (C) in 2-month-old and 18-month-old brains. (D-F) Scatter plots of averaged vascular length density (m/mm^3) (D), vascular branching density ($1/\text{mm}^3$) (F), and vascular radii (μm) between 2-month-old (x axis) and 18-month-old (y axis) brains across different brain regions. Areas with statistically significant differences were highlighted with magenta boxes. (G-I) Scatter plots of the isocortex data for averaged vascular length density (G), vascular branching density (H), vascular radii (I) between 2-month-old (x axis) and 18-month-old (y axis) brains. Isocortical areas are color coded based on grouping in J. The solid yellow line represents $y=x$ and the dotted line on either side represents a 10% difference from the solid yellow line. (J) Isocortical flatmap with Allen CCF border lines and region-based color-coding. Y axis: Bregma anterior-posterior (A-P) coordinates, X axis: the azimuth coordinate represents the physical distance by tracing the cortical surface on the coronal cut. (K) Averaged vascular length density of different cortical layers in the flatmap between 2-month-old and 18-month-old brains. A white arrow highlights the significant decrease of vascular length density in the layer 6 cortical layers. (L-M) 250 μm maximum intensity projection images of the primary somatosensory cortex (L) and the infralimbic cortex (M) with vascular tracing (green on the right side) between 2-month-old and 18-month-old brains. Note the significant reduction of vasculature in the deep layer. (N) Both vascular length and branching density showed significant reductions in layer 6. Brain region abbreviations can be found in Supplementary data 1 or Allen atlas at <https://atlas.brain-map.org/atlas?atlas=602630314>.

Figure 3

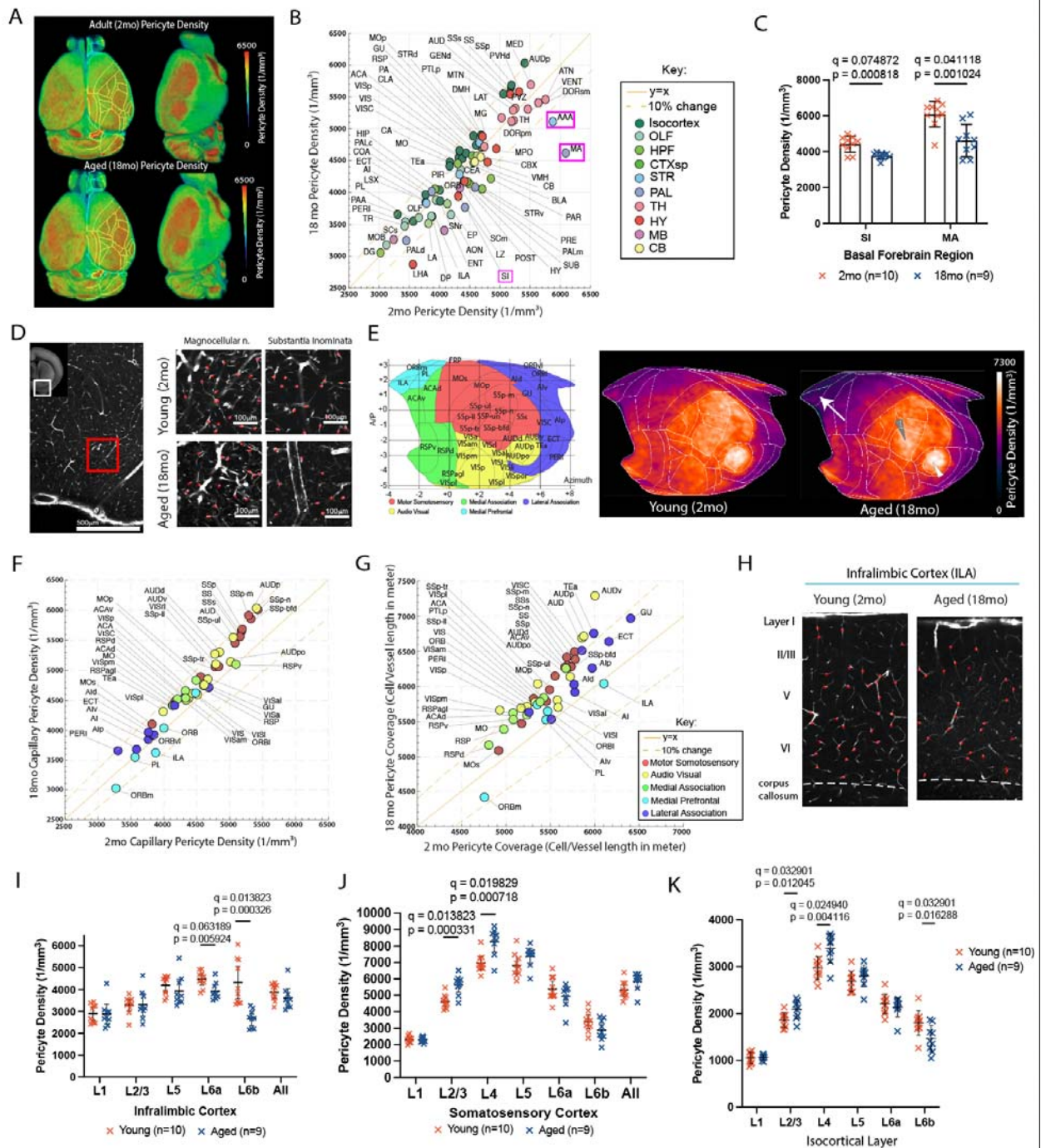


Figure 3. Aged brain showed selective reduction of capillary pericytes in the basal forebrain area and the deep cortical layer

(A) Averaged capillary pericyte density in 2-month-old (n=10) and 18-month-old (n=9) PDGFR β -Cre;Ai14 mouse brains that are registered to the Allen CCF. (B) A scatter plot of capillary pericyte density between 2-month-old (x axis) and 18-month-old (y axis). Brain areas are color coded based on the Allen CCF ontology. Brain areas with significant changes were highlighted with magenta-colored boxes. The solid yellow line represents the value for y=x and the yellow dotted lines on either side of the solid yellow line represent a 10% difference from the

solid yellow line. **(C)** Bar graphs of capillary pericyte density in the substantia innominata and magnocellular nucleus between 2-month-old and 18-month-old brains. **(D)** Representative images of the basal forebrain (left) and higher resolution examples of the magnocellular nucleus and substantia innominata in 2-month-old and 18-month-old brains. Red dots represent detected pericyte cell bodies in each respective region. **(E)** The isocortical flatmap (left) and averaged capillary pericyte densities plotted in the flatmap from 2-month-old and 18-month-old brains. **(F-G)** Scatter plots of capillary pericyte density **(F)** and pericyte coverage (pericyte density per vascular length density; **G**) in isocortical areas. **(H)** Representative images of capillary pericyte density in the infralimbic cortex from 2-month-old and 18-month-old brains. **(I-K)** Layer specific capillary pericyte densities from the infralimbic cortex **(I)**, the somatosensory cortex **(J)**, and across all isocortical areas **(K)**. Note the significant density reduction in the deep cortical layers. All q values obtained from multiple comparison correction by false discovery rate are reported in each graph as well as the uncorrected p-value.

Figure 4

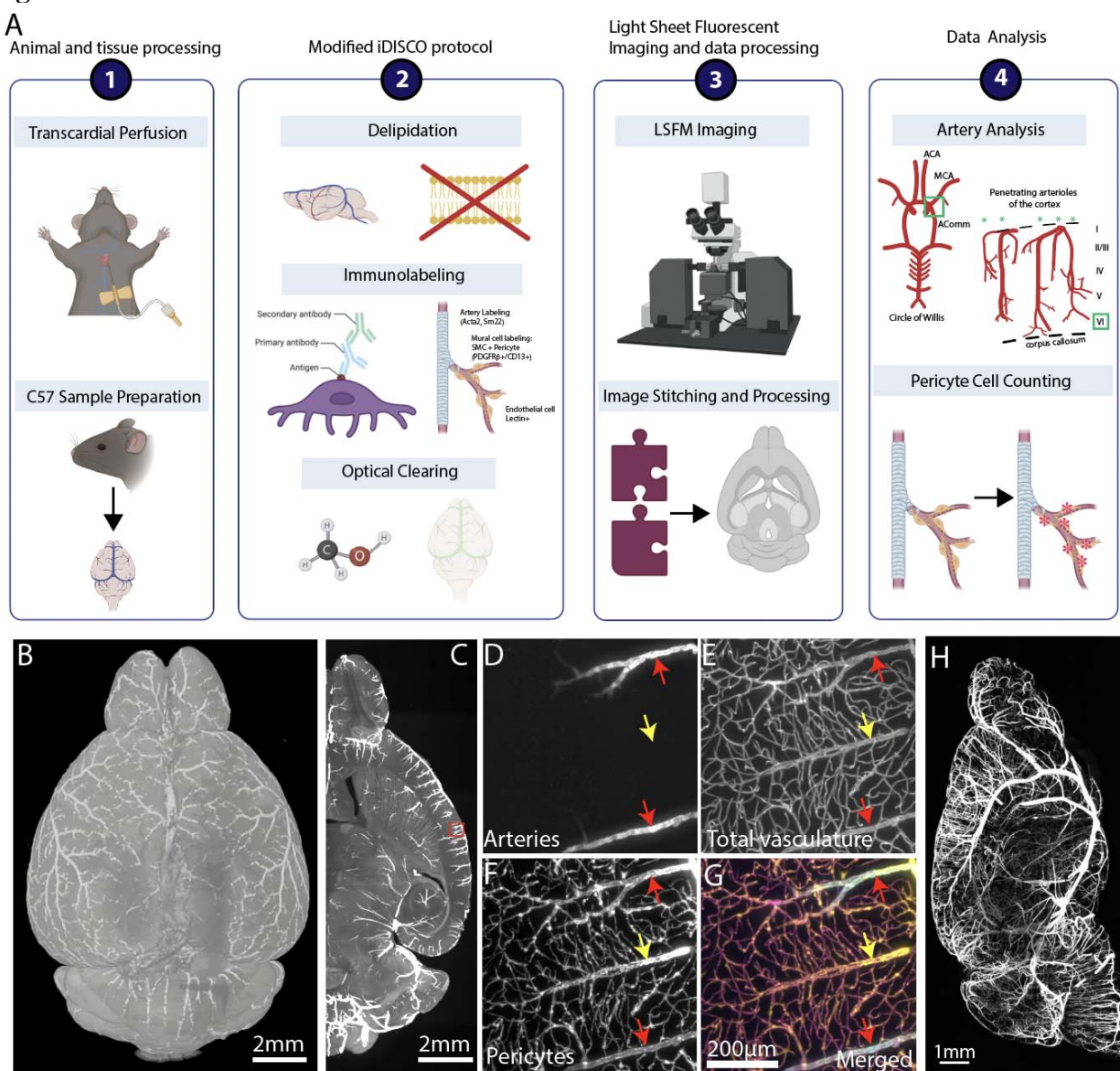


Figure 4. Tissue clearing and 3D immunolabeling with LSFM imaging to examine different vascular compartments and mural cells in the same brain

(A) The steps of brain clearing, whole brain immunolabeling, and light sheet fluorescent microscopy (LSFM) pipeline are outlined in order. **1.** Brain sample collection with transcardial perfusion. **2.** Modified iDISCO protocol including delipidation, immunolabeling for arteries, whole vasculature, and pericytes, and optical clearing. **3.** LSFM imaging and data processing to visualize cleared brains at cellular resolution. **4.** Data analysis such as arteriole geometry analysis and pericyte counting. (B) 3D reconstruction of a brain with artery staining by LSFM imaging. (C) Max projection of the 500 μm thick z stack of the artery staining. (D-G) Zoom-in images of the red box area from (C). (D) artery staining in the green channel, (E) lectin based total vasculature staining in the red channel, (F) pericyte staining in the far-red channel, (G) a merged image of pseudo-colored arteries (blue), total vasculature (green), and pericyte (red). (H) Maximum projection of the artery channel in a brain hemisphere.

Figure 5

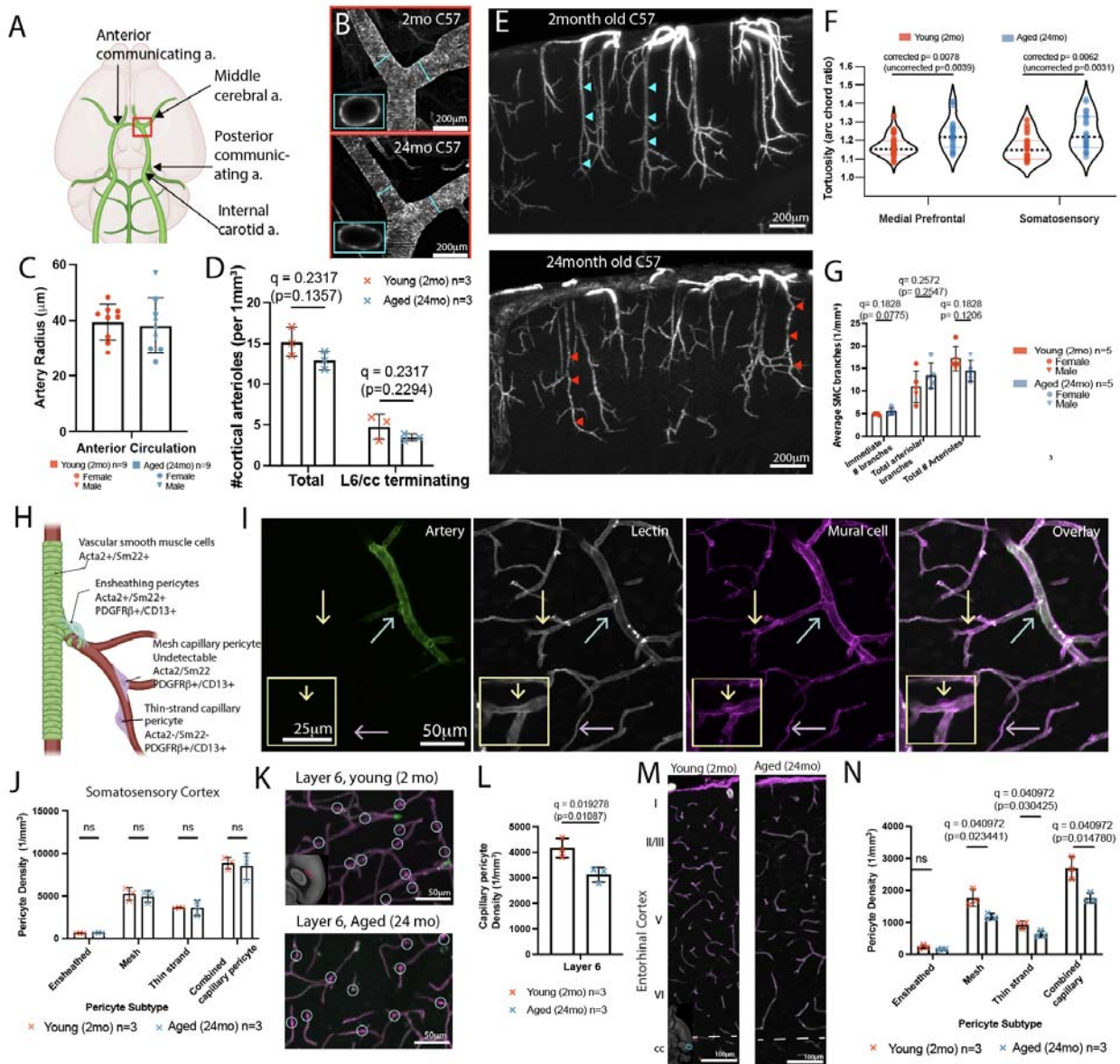


Figure 5. Aging induces significant arteriole remodeling and selective pericyte density reduction.

(A) Schema of main arteries of the circle of Willis at the ventral surface of the brain. (B) Artery specific labeling of the middle cerebral artery branching area (red box area in H) from 2-month-old and 24-month-old brains. (C) Artery radii do not show a significant difference between the two age groups. (D) The number of both total and deep layer 6 reaching penetrating cortical arteriole did not show a significant difference between the two age groups. (E) Representative 600 µm MIPs of artery labeling in the somatosensory area of a young (top) and an aged (bottom) brain. Note tortuous arterioles in the old brain (red arrowheads) compared to straight ones in the young brain (light blue arrowheads). (F) Old brains showed significantly tortuous arterioles in the medial prefrontal and somatosensory cortices. Data from 3 animals for both young and aged groups. (G) Both immediate and total arteriole branch numbers show no significant differences between the two age groups. (H) Different pericyte subtypes with immuno markers and their

position in the vascular order. **(I)** Submicron resolution LSM images with artery labeling, whole vasculature labeled with lectin and mural cell labeling with PDGFR β and CD13 antibodies. The cyan arrow for an ensheathing pericyte, the yellow arrow for a mesh capillary pericyte, and the purple arrow for a thin-strand capillary pericyte. **(J)** Manual cell counting did not show any significant difference in the somatosensory cortex between the two age groups. **(K-L)** However, layer 6 of the somatosensory cortex **(K)** showed a significant reduction in pericyte density **(L)**. **(M-N)** The entorhinal cortex **(M)** showed a significant reduction of capillary pericytes **(N)**. All q values obtained from multiple comparison correction by false discovery rate and uncorrected p-value are reported in each graph, except (F) with Bonferroni correction.

Figure 6

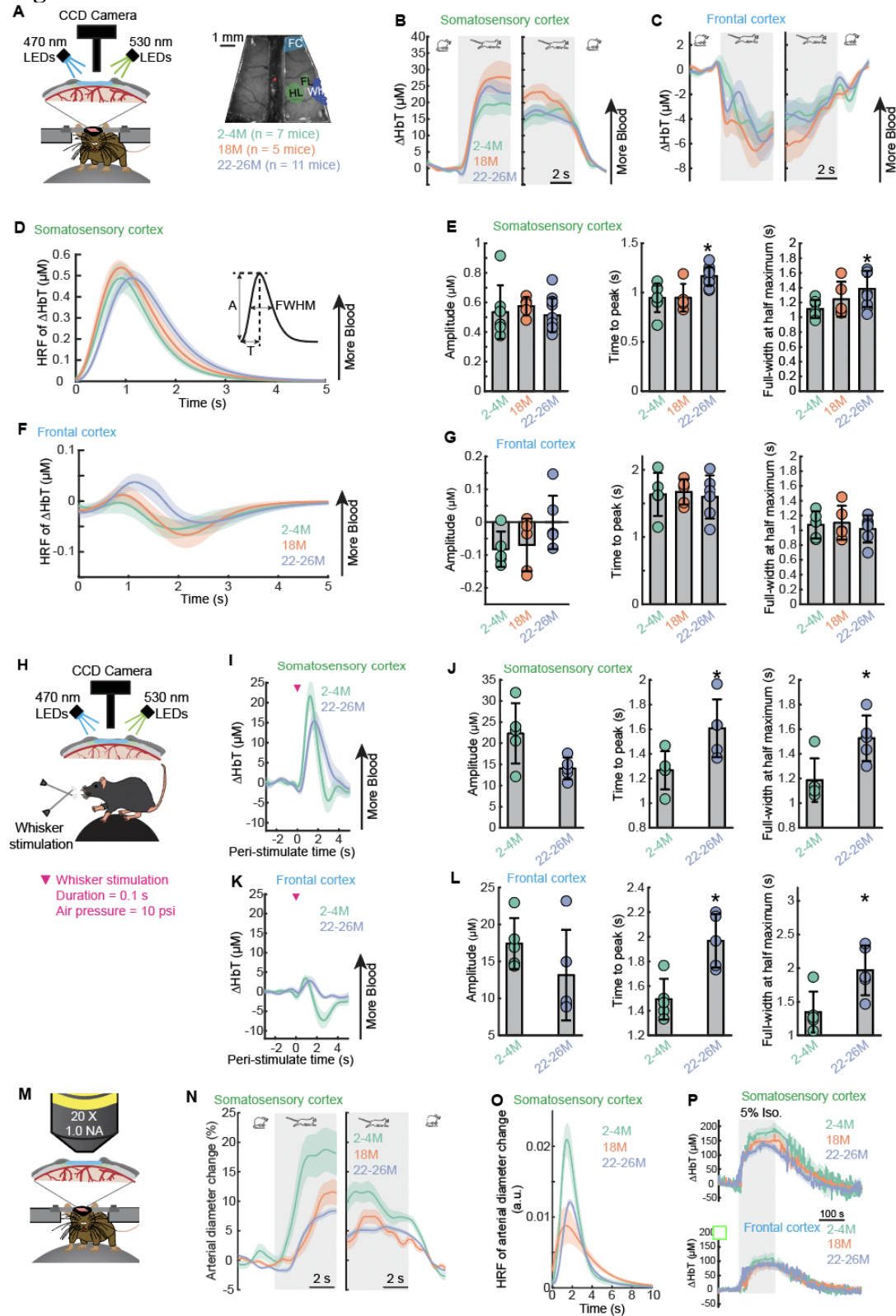


Figure 6. Delayed cortical hemodynamic responses to voluntary locomotion and whisker stimulation is delayed in normal aging.

(**A**) Left, schematic of the experimental setup for IOS imaging during voluntary locomotion. Right, an image of thin-skull window and corresponding anatomical reconstruction; scale bar = 1 mm. FC, frontal cortex; FL/HL, forelimb/hindlimb representation of the somatosensory cortex; Wh, vibrissae cortex. (**B**) Population average of locomotion onset (left) and offset (right) triggered average of ΔHbT responses in FL/HL across different age groups. (**C**) As in (**B**) but for FC. (**D**) Hemodynamic response function (HRF) of ΔHbT in the FL/HL across different age groups. (**E**) Quantification of HRF of ΔHbT in the FL/HL: amplitude (A, left), time to peak (T, middle), and full-width at half maximum (FWHM, right). (**F**) As in (**D**) but for FC. (**G**) As in (**E**) but for FC. (**H**) Schematic of the experimental setup for IOS imaging during whisker stimulation. (**I**) Average population responses of ΔHbT to contralateral whisker stimulation in the FL/HL across different age groups. (**J**) Quantification of the whisker stimulation evoked responses of ΔHbT in the FL/HL: amplitude (left), time to peak (middle), and full-width at half maximum (right). (**K**) As in (**I**) but for FC. (**L**) As in (**J**) but for FC. (**M**) Schematic of the experimental setup for 2PLSM imaging during locomotion. (**N**) Population average of locomotion onset (left) and offset (right) triggered average of arteriole diameter responses in FL/HL across different age groups. (**O**) Hemodynamic response function (HRF) of arteriole diameter changes in the FL/HL across different age groups. (**P**) Population average of ΔHbT responses to inhalation of 5% isoflurane in the FL/HL (top) and FC (bottom) across different age groups. Solid lines and shaded areas in (**B**, **C**, **D**, **F**, **I**, **K**, **N**, **O**, **P**) denote mean \pm SEM, respectively. Data are shown as mean \pm SD in all other graphs.

Figure 7

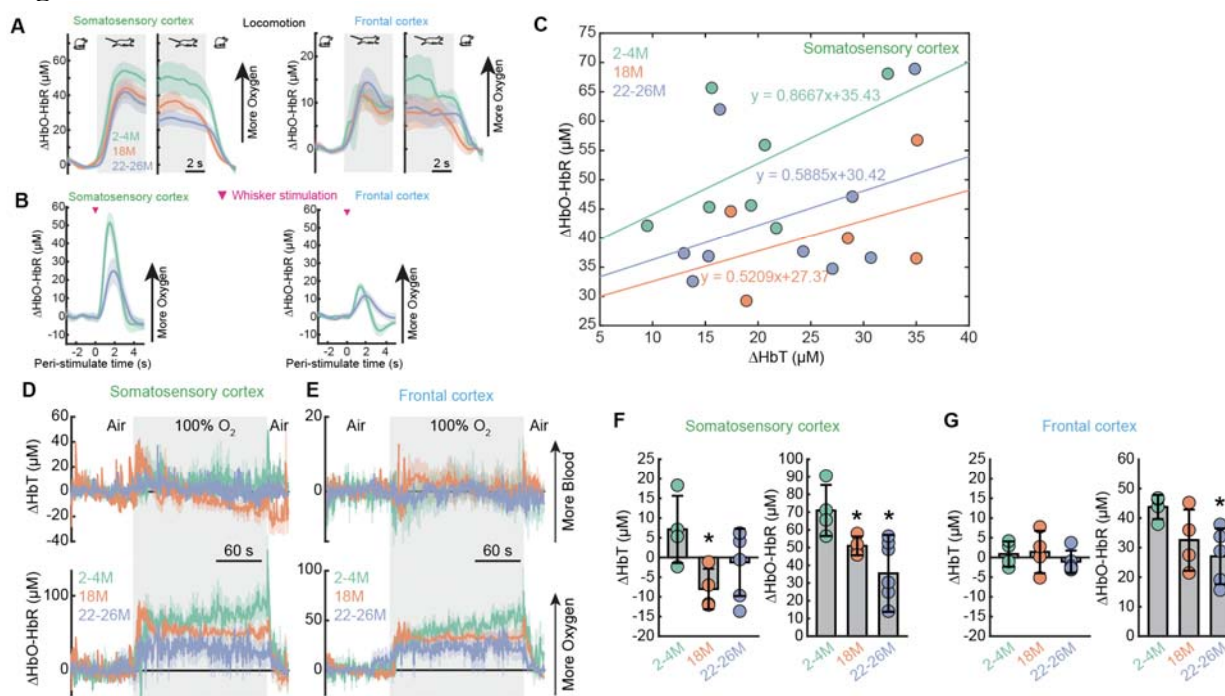


Figure 7. Oxygen carrying capacity of the blood is reduced by aging.

(A) Population average of locomotion onset and offset triggered average of brain oxygenation ($\Delta\text{HbO-HbR}$) responses in FL/HL and FC across different age groups. (B) Average population responses of $\Delta\text{HbO-HbR}$ to contralateral whisker stimulation in the FL/HL and FC across different age groups. (C) Relationship between locomotion evoked change in ΔHbT and $\Delta\text{HbO-HbR}$, 2-5 s after the onset of locomotion, across different age groups, in FL/HL. (D) Population average of ΔHbT (top) and $\Delta\text{HbO-HbR}$ (bottom) responses to inhalation of 100% oxygen in the FL/HL across different age groups. (E) As in (D) but for FC. (F) Group average of fractional changes of ΔHbT (left) and $\Delta\text{HbO-HbR}$ (right) in response to 100% oxygen in FL/HL across different age groups. (G) As in (F) but for FC. Solid lines and shaded areas in (A, B, E, F) denote mean \pm SEM, respectively. Data are shown as mean \pm SD in all other graphs.

Figure 8

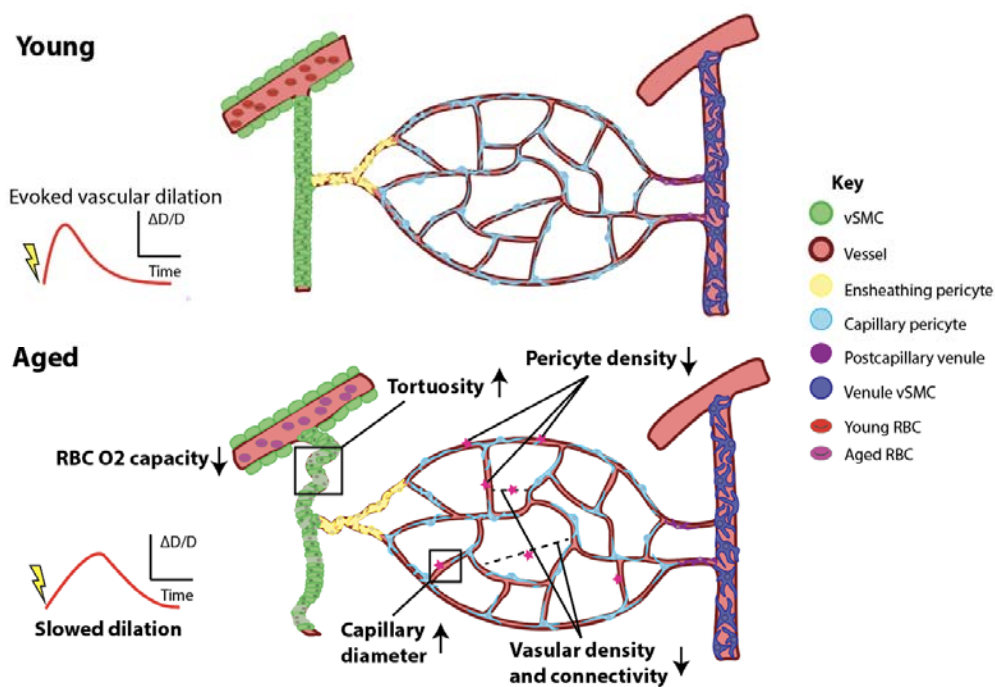


Figure 8. Summary of changes in aged brains

Aged brains show reduced vascular length and branching density, increased radii, reduced pericyte density, slowed vascular response time, and lower oxygen carrying capacity in the blood compared to young brains.